Available online at www.sciencedirect.com

ScienceDirect

Geochimica et Cosmochimica Acta 127 (2014) 204–220

Geochimica et Cosmochimica Acta

www.elsevier.com/locate/gca

The role of Mg in the crystallization of monohydrocalcite

Juan Diego Rodriguez-Blanco [a,b], Samuel Shaw [a,c], Pieter Bots [a,c], Teresa Roncal-Herrero [a], Liane G. Benning [a,*]

[a] School of Earth and Environment, University of Leeds, Leeds LS2 9JT, United Kingdom
[b] Now at the Nano Science Center, University of Copenhagen, 2100 Copenhagen, Denmark
[c] School of Earth, Atmospheric and Environmental Sciences, The University of Manchester, Oxford Road, Manchester M13 9PL, United Kingdom

Received 17 February 2013; accepted in revised form 26 November 2013; Available online 6 December 2013

Abstract

Monohydrocalcite is a member of the carbonate family which forms in Mg-rich environments at a wide range of Mg/Ca ratios $Mg^{2+}_{aq}/Ca^{2+}_{aq} \geq 0.17 < 65$. Although found in modern sedimentary deposits and as a product of biomineralization, there is a lack of information about its formation mechanisms and about the role of Mg during its crystallization. In this work we have quantitatively assessed the mechanism of crystallization of monohydrocalcite through *in situ* synchrotron-based small and wide angle X-ray scattering (SAXS/WAXS) and off-line spectroscopic, microscopic and wet chemical analyses. Monohydrocalcite crystallizes via a 4-stage process beginning with highly supersaturated solutions from which a Mg-bearing, amorphous calcium carbonate (ACC) precursor precipitates. This precursor crystallizes to monohydrocalcite via a nucleation-controlled reaction in stage two, while in stage three it is further aged through Ostwald-ripening at a rate of 1.8 ± 0.1 nm/$h^{1/2}$. In stage four, a secondary Ostwald ripening process (66.3 ± 4.3 nm/$h^{1/2}$) coincides with the release of Mg from the monohydrocalcite structure and the concomitant formation of minor hydromagnesite. Our data reveal that monohydrocalcite can accommodate significant amounts of Mg in its structure ($\chi_{MgCO3} = 0.26$) and that its Mg content and dehydration temperature are directly proportional to the saturation index for monohydrocalcite (SI_{MHC}) immediately after mixing the stock solutions. However, its crystallite and particle size are inversely proportional to these parameters. At high supersaturations ($SI_{MHC} = 3.89$) nanometer-sized single crystals of monohydrocalcite form, while at low values ($SI_{MHC} = 2.43$) the process leads to low-angle branching spherulites. Many carbonates produced during biomineralization form at similar conditions to most synthetic monohydrocalcites, and thus we hypothesize that some calcite or aragonite deposits found in the geologic record that have formed at high Mg/Ca ratios could be secondary in origin and may have originally formed via a metastable monohydrocalcite intermediate.

1. INTRODUCTION

A variety of calcium carbonate minerals are stable at Earth surface conditions. These include the common polymorphs calcite, vaterite and aragonite, and the less common and hydrated phases monohydrocalcite ($CaCO_3 \cdot H_2O$) and ikaite ($CaCO_3 \cdot 6H_2O$). Monohydrocalcite forms in a variety of modern natural environments including saline spring waters (Ito, 1993), marine polar systems (e.g., Antarctic lakes, or Ikka Fjord, Greenland; Bird et al., 1991; Dahl and Buchardt, 2006), basaltic caves (Broughton, 1972; Onac, 2000; Léveillé et al., 2000), cold/humid mine galleries and lacustrine deposits. Representative of the latter environment is for example, the oldest known monohydrocalcite, 800 ka. (Solotchina et al. (2009), that was found in deep sediments at Lake Hovsgol, NW Mongolia. Other lacustrine examples include Lake Kivu in Africa, or Lake Fellmongery and Lake Butler in S. Australia

* Corresponding author. Tel.: 44 (0)113 343 5220.
E-mail addresses: jblanco@nano.ku.dk (J.D. Rodriguez-Blanco), L.G.Benning@leeds. ac.uk (L.G. Benning).

0016-7037/$ - see front matter
http://dx.doi.org/10.1016/j.gca.2013.11.034

(Stoffers and Fischbeck, 1974 and Taylor, 1975). Monohydrocalcite is usually found in association with other carbonates like Mg-calcite, aragonite, Ca-rich dolomite ($CaMg(CO_3)_2$) or Mg carbonates like hydromagnesite ($Mg_5(CO_3)_4(OH)_2{\cdot}4H_2O$) and nesquehonite ($MgCO_3{\cdot}3H_2O$) (Fischbeck and Müller, 1971; Broughton, 1972; Nishiyama et al., 2013). Monohydrocalcite is also formed as a product of biomineralization by certain molluscs (Lowenstam, 1981), flatworms (calcareous corpuscles of Platyhelminthes; Señorale-Pose et al., 2008), vertebrates (otoliths; Carlström, 1963), guinea pigs (bladder stones; Skinner et al., 1977) or is even found as a decay product in Saguaro cacti (Garvie, 2003, 2006). It has also been described associated with algae (Taylor, 1975) or halo bacilli (Rivadeneyra et al., 2004). However, despite its occurrence in a wide variety of systems little is known about the mechanism and kinetics of its formation pathway.

At Earth surface temperatures and pressures, monohydrocalcite is thermodynamically unstable relative to anhydrous calcite and aragonite. In the presence of a Mg-free aqueous fluid it will slowly (>2 days at 100 °C, several days/weeks at ambient temperature) transform to calcite (Stoffers and Fischbeck, 1974; Taylor, 1975). Yet, even minor concentrations of aqueous magnesium will lead to its transformation to aragonite over 25 days at ambient temperatures (Brooks et al., 1950; Kamiya et al., 1977; Dahl and Buchardt, 2006; Munemoto and Fukushi, 2008; Fukushi et al., 2011). This effect is believed to be due to the inhibiting effect of Mg^{2+} on calcite crystallization (Mucci and Morse, 1983; Davis et al., 2000; Chen et al., 2004; Bots et al., 2011). The instability of monohydrocalcite with respect to calcite and aragonite explains the relatively low abundance of this phase within modern environmental systems and the geological record.

The mechanism of monohydrocalcite crystallization in many systems is unknown, but some studies indicate that it can form from an amorphous precursor (Kamiya et al., 1977; Loste et al., 2003; Fukushi et al., 2011; Nishiyama et al., 2013). Such a crystallization pathway has been shown to be common for many Ca–Mg carbonates (e.g., vaterite, aragonite, dolomite; Bots et al., 2012; Rodriguez-Blanco et al., 2012, 2009; Sand et al., 2012; Ihli et al., 2012), and other carbonate and phosphate systems (Roncal-Herrero et al., 2009, 2011; Vallina et al., 2013), but this amorphous to crystalline transition is not ubiquitous (Van Driessche et al., 2012). In the carbonate system, these studies have shown that the transformation of the amorphous calcium carbonate (ACC) precursor to stable crystalline phases (i.e., vaterite, dolomite) occurs via a nucleation dominated (spherulitic) growth mechanism. Despite its presence in a variety of natural settings and biominerals, a quantitative evaluation of the kinetics and mechanisms of monohydrocalcite formation from an amorphous precursor is lacking.

Monohydrocalcite has a hexagonal structure with space group $P3_112$ and an atomic structure consisting of irregular 8-folded Ca–O polyhedra, with a central Ca^{2+} ion surrounded by carbonate groups and water molecules (Effenberger, 1981; Neumann and Epple, 2007; Swainson, 2008). The presence of the water makes its structure more open and less dense compared to anhydrous $CaCO_3$ (e.g., calcite or aragonite). Interestingly, monohydrocalcite is described as a pure 'calcium' carbonate phase in mineralogical databases, but a number of studies have shown that Mg is ubiquitous in all synthetic and natural monohydrocalcite samples (Mg/Ca = ~0.01–0.53; Hull and Turnbull, 1973; Taylor, 1975; Neumann and Epple, 2007; Nebel et al., 2008; Fukushi et al., 2011; Nishiyama et al., 2013). The Mg content of monohydrocalcite is likely to be linked to the overall fluid chemistry and in particular to the Mg contents of the fluid in which it forms. In both natural and most synthetic monohydrocalcites the presence of high concentrations of Mg relative to Ca in the precipitating solution ($Mg^{2+}_{aq}/Ca^{2+}_{aq} \geq 0.17 < 65$) is a prerequisite for its formation (e.g., Neumann and Epple, 2007; Munemoto and Fukushi, 2008; Last et al., 2010; Kimura and Koga, 2011). Recently, Nishiyama et al. (2013) have also shown that the crystallinity and particle size of synthetic monohydrocalcite decrease with Mg content. This clearly shows that Mg is a key component in monohydrocalcite, and must be present in the fluids in which it crystallizes. However, the exact mechanisms by which Mg controls the formation and stability of monohydrocalcite are unknown.

This study aims to determine the mechanism of monohydrocalcite crystallization in solution via an ACC precursor. We evaluate the role of Mg during this process and test the hypothesis that a nucleation-dominated process controls the formation of monohydrocalcite from the Mg-containing precursor ACC. This has been done through a series of experiments where the nucleation and crystallization of monohydrocalcite from Mg doped-ACC was followed *in situ* and in real time with synchrotron-based X-ray scattering combined with microscopic and wet chemical characterization of the solids and solutions throughout the reaction. Our results demonstrate that the formation of monohydrocalcite takes place via a 4-stage process that starts with the precipitation of an Mg-rich ACC precursor. This precursor crystallizes in stage two to monohydrocalcite through a nucleation-controlled dissolution-reprecipitation reaction. In stage three Ostwald-ripening dominates, while in stage four, a secondary monohydrocalcite crystallization, also through Ostwald ripening, occurs concomitantly with the loss of some of its structural Mg. We also show that, depending on the aqueous Mg/Ca ratio and supersaturation, monohydrocalcite can accommodate large amounts of Mg in its structure (up to ~25% Ca replaced by Mg) and that the aqueous chemistry of the starting solution controls the crystallite size, unit-cell dimensions and particle size/shape of the forming monohydrocalcite. Based on these findings we discuss the implications of this monohydrocalcite crystallization pathway, on its occurrence in various natural settings and as a biomineral.

2. EXPERIMENTAL

Experiments were carried out at 21 °C by rapid addition (under constant and vigorous stirring) of a $CaCl_2/MgCl_2$ solution (700 mM $CaCl_2$; 300 mM $MgCl_2$; Ca/Mg ratio of 7/3) to a 1000 mM Na_2CO_3 solution to achieve a $(Ca + Mg)/CO_3$ ratio of 1/1. In all cases immediately upon mixing a white gel precipitated. The crystallization of this

white gel was followed on-line using *in situ* and time resolved small and wide angle X-ray Scattering (SAXS/WAXS) on beamline I22 (Diamond Light Source Ltd., UK). Solutions were mixed using a stopped-flow apparatus (Bio-Logic, Paris, France) and the resulting white suspensions were continuously circulated with a peristaltic pump through a capillary cell in line with the synchrotron beam. Simultaneous SAXS (RAPID detector; Marchal et al., 2009) and WAXS (HOTWAXS detector; Bateman et al., 2007) patterns were collected over 12 h at 1 min/frame. The time resolved scattering patterns were detector-response corrected, and background subtracted using a scattering pattern from the starting Na_2CO_3 solution. Individual WAXS patterns were fit using XFIT (Cheary and Coelho, 1992) and the areas under the Bragg peaks normalized to values from 0 to 1 to express the degree of reactions (α) as a function of time (Rodriguez-Blanco et al., 2011). Crystallite size was calculated from the Bragg peak full-width half-maximum (FWHM) using the Scherrer equation (Scherrer, 1918) and the unit cell parameters were determined with TOPAS (Coelho, 2006), using the Swainson (2008) model for the monohydrocalcite structure.

The variations in the scattering peak position in the SAXS patterns were used to derive the changes in the particle sizes of the solids throughout the experiments via the expression:

$$d = 2\pi/q \quad (1)$$

where d (nm) is particle diameter and q (nm^{-1}) is the scattering vector (de Moor et al., 1999a; de Moor et al., 1999b). These particle size results were also cross-validated by whole SAXS pattern fitting using GNOM (Svergun, 1992).

Experiments equivalent to the online SAXS/WAXS experiments (i.e., 1000 mM Na_2CO_3 solution mixed with a 700 mM $CaCl_2$ and 300 mM $MgCl_2$ solution) were performed to follow the reaction process via time-dependent solid characterization and solution analyses. At specific time steps aliquots of the reacting suspension were removed and immediately vacuum filtered (0.2 μm polycarbonate membranes). The resulting solids were washed with water and isopropanol following Rodriguez-Blanco et al. (2008). An aliquot of each solid sample was dissolved in 0.1 M HCl and analyzed together with the corresponding solution samples for aqueous Ca and Mg concentrations ($[Ca^{2+}_{aq}]$ and $[Mg^{2+}_{aq}]$) using ion chromatography (Dionex LC 220) following Bots et al. (2011). Throughout all experiments the pH was recorded at a 10 s time resolution using an Orion pH meter and WinWedge v3.4.1 software (TAL technologies) with a precision of 0.001. Finally, the total carbonate concentration in solution was determine by assuming that all Ca and Mg precipitated formed Ca/Mg carbonate, therefore the moles of Ca + Mg removed form solution must equal the total moles of carbonate removed. The total carbonate was then calculated from the difference between the initial concentration and the amount removed at each time point. From these solution data the saturation indexes (SI) with respect to different Ca and Mg-bearing carbonates were calculated using PHREEQC (Parkhurst, 1995) and are presented in Table 1. This was done using the Pitzer activity coefficient models (Pitzer, 1979) and two solubility products, $K_{sp(MHC)}$, for monohydrocalcite ($10^{-7.60}$; Hull and Turnbull, 1973) and ($10^{-7.05}$; Kralj and Brečević, 1995). The saturation index of monohydrocalcite is defined as:

$$SI_{MHC} = \log \frac{a_{Ca^{2+}} \cdot a_{Co_3^{2-}}}{K_{sp(MHC)}} \quad (2)$$

To determine the effect of initial supersaturation (i.e. saturation index of the aqueous solution for monohydrocalcite immediately after mixing the stock solutions) on the crystallization reaction, experiments were also performed following the same procedure but starting at different initial supersaturations with respect to monohydrocalcite, yet keeping a 1/1 (Ca + Mg)/CO_3 ratio (Table 2) in all cases. Using the $[Ca^{2+}_{aq}]$ and $[Mg^{2+}_{aq}$ concentrations obtained from the analyses of the dissolved solids, the molar fraction of $MgCO_3$ in each solid sample, χ_{MgCO3}, was calculated following:

$$\chi_{MgCO_3} = \frac{M_{MgCO_3}}{M_{MgCO_3} + M_{CaCO_3}} \quad (3)$$

where M_{MgCO3} and M_{CaCO3} correspond to the molar concentration of $MgCO_3$ and $CaCO_3$, respectively.

The mineralogy of the solids from off-line experiments was characterized by powder X-ray diffraction (PXRD) using a Bruker D8 X-ray Diffractometer (CuKα1, 5–90° two theta, 0.001°/step; 0.1 or 1 s/step). The PXRD patterns were also used to derive the crystallite size using the Scherrer equation (Scherrer, 1918). All samples were imaged by high-resolution transmission electron microscopy (HR-TEM; Philips CM200 field emission gun TEM equipped with a Gatan Imaging Filter, GIF-200 and a Gatan camera for selected area electron diffraction, SAED, pattern collection) or scanning electron microscopy (SEM; LEO 1530 Gemini). Finally, the water content of the samples was determined using thermogravimetric analyses (TGA, Mettler Toledo, 25–800 °C in air, 10 °C/min). The total water content for the initial white precipitate was calculated from the difference in weight between 25 and 550 °C in accordance with the method of Radha et al. (2012) for determining the water content of ACC. For crystalline samples the difference in weight between 100 and 550 °C was used, in accordance with the method of Hull and Turnbull (1973) for determining the water content of monohydrocalcite.

3. RESULTS AND DISCUSSION

Our data revealed that over the 12 h of our experiments monohydrocalcite formed through a multi-stage crystallization pathway. The first stage of the reaction was characterized by the formation of a Mg-bearing amorphous calcium carbonate phase. In stage two, this amorphous phase crystallized to nanoparticulate monohydrocalcite. The rate of crystallization slowed considerably during stage three, coincident with only minor changes in the solution composition (e.g., pH). Finally, in the fourth stage of the reaction secondary growth of the nanoparticulate monohydrocalcite was observed. This was accompanied by the simultaneous decrease in $[Mg^{2+}_{aq}]$ and the formation of minor amounts of hydromagnesite ($Mg_5(CO_3)_4(OH)_2{\cdot}4H_2O$). Each of these four stages is described in detail below:

Table 1
Evolution of the aqueous solution composition, the magnesium content in the solids ($_{MgCO3}$) and the solid mineralogy during the course of a typical experiment. Saturation indexes for monohydrocalcite, hydromagnesite and nesquehonite (SI_{MHC} and SI_{HMgS}, SI_{nesq}) were calculated from the measured pH and [$Ca^{2+}{}_{aq}$] and [$Mg^{2+}{}_{aq}$] values combined with the solubility products for monohydrocalcite reported by (1) Hull and Turnbull (1973), and (2) Kralj and Brecevic (1995) and those for hydromagnesite and nesquehonite from Johnson et al. (2000). Average particle sizes were evaluated from the SAXS data or from photomicrographs.

Stage	Time (h)	pH	[$Ca^{2+}{}_{aq}$] (mM)	[$Mg^{2+}{}_{aq}$] (mM)	χ_{MgCO3} solid	Mineralogy	Particle sizes from SAXS/Crystallite sizes from Scherrer (nm)	Particle sizes from TEM imaging (nm)	SI_{MHC} (1)	SI_{MHC} (2)	SI_{HMgS}	SI_{nesq}
Pre-mixing	0	–	350	150	–	–	40–60/–		3.89	3.34	13.06	1.17
I	0.083	9.239	1.25 ± 0.05	28.17 ± 1.26	0.258 ± 0.005	Mg–ACC	40–60/–	~40	0.82	0.27	5.38	0.03
	0.5	9.217	0.84 ± 0.04	27.75 ± 1.68	0.261 ± 0.005		43/–		0.66	0.11	5.55	0.04
II	–	–	–	–	–	–	–	–	–	–	–	–
III	2.5	9.214	0.32 ± 0.02	28.08 ± 1.57	0.260 ± 0.005	MHC	10/15	28 ± 7 (L) × 20 ± 5 (W)	0.23	−0.32	5.49	0.04
	3	9.203	0.51 ± 0.03	31.05 ± 1.48	0.250 ± 0.004		11/15		0.46	−0.09	5.8	0.11
	5	9.167	0.68 ± 0.03	34.59 ± 1.14	0.247 ± 0.005		11/16		0.62	0.07	6.1	0.18
	7	9.171	0.62 ± 0.06	35.62 ± 2.00	0.249 ± 0.016		–/17		0.58	0.03	6.06	0.19
	8	9.111	0.29 ± 0.01	25.47 ± 0.93	0.266 ± 0.004		–/17.5		0.14	−0.41	4.99	−0.05
IV	9	8.893	0.09 ± 0.01	12.64 ± 0.75	0.274 ± 0.005	MHC + HMgS	15/22.5		−0.6	−1.15	2.36	−0.60
	10	8.646	0.08 ± 0.00	12.83 ± 0.39	–		35/37.5	155 ± 80 (L) × 40 ± 30 (W)	−0.76	−1.31	1.42	−0.70
	12	8.609	0.09 ± 0.00	13.12 ± 0.54	0.283 ± 0.005		45/45		−0.85	−1.4	0.27	−0.85

Table 2
Initial stock solution concentrations, and corresponding calculated monohydrocalcite saturation index (SI_{MHC}) for the solution immediately after mixing for each experiment. The first line represents the conditions used in the on-line SAXS/WAXS experiments. The mineralogy, Scherrer crystallite size and Mg (χ_{MgCO3}), and H_2O content of the solid products after 2 h of reaction are also presented. The saturation index of monohydrocalcite was calculated using the solubility product from Hull and Turnbull (1973).

$Na_2CO_{3(ini)}$ (mM)	$[Ca^{2+}{}_{aq}]_{(ini)}$ (mM)	$[Mg^{2+}{}_{aq}]_{(ini)}$ (mM)	SI_{MHC} ($t = 0$ s)	Mineralogy from PXRD	Scherrer crystallite size (average) (nm)	χ_{MgCO3} solid *	H_2O content
500	350	150	3.89	MHC	16	0.164	0.99
250	175	75	3.52	MHC	17	0.180	1.03
200	140	60	3.41	MHC	-	0.143	1.00
100	70	30	3.08	MHC	-	0.061	0.97
50	35	15	2.76	MHC	35	0.028	0.95
25	17.5	7.5	2.43	MHC	35	0.017	0.93
12.5	8.75	3.75	2.10	Mg-Calcite	43	0.073	0
5	3.5	1.5	1.63	Mg-Calcite	131	0.032	0

* Errors for χ_{MgCO3} of solids are in all cases lower than 0.002.

In ***Stage I*** of the reaction a white gel precipitated immediately upon solution mixing. The PXRD patterns of this gel (Fig. 1a, lower pattern) showed no Bragg peaks and only three humps located at 2θ (= 1.54 Å) 17°, 31° and 45°, indicating the solid is poorly-ordered. These three broad humps (asterisks in Fig. 1a), are located at the same positions as those observed for Mg-free amorphous calcium carbonate (ACC; Rodriguez-Blanco et al., 2008). Based on the chemical analyses of this amorphous phase (Table 1, 0.83 h sample) and the TGA results, the formula for this compound was determined to be $Ca_{0.74}Mg_{0.26}CO_3{\cdot}1.18H_2O$. In line with previous studies where the incorporation of Mg into ACC has been quantified (Nebel and Epple, 2008; Wang et al., 2009; Rodriguez-Blanco et al., 2012), we will term this poorly-ordered phase, Mg-ACC, following the notation of Günther et al. (2005). Throughout this first stage, Mg-ACC was the only solid phase present. In both the on-line and off-line experiments and regardless of conditions, the Mg-ACC started to crystallize after approximately 50 min to 1 h, initiating ***Stage II***. During this stage the background intensity in the PXRD patterns decreased with time, and Bragg peaks for monohydrocalcite formed, grew and sharpened (Fig. 1a). The on-line time resolved WAXS data (Fig. 1b) shows the simultaneous growth of the monohydrocalcite (1 1 0), (1 1 1), (3 0 0) and (3 0 1) peaks, after ~1 h. The whole reaction is clearly illustrated when the change in area for a specific Bragg peak, expressed as the degree of reactions (α), is plotted as a function of time (Fig. 2). Stage II of the reaction lasted for about 1 h and was characterized by the rapid increase in monohydrocalcite peak area. After the fast growth in stage II, a much slower growth phase, between ~2 and 8 h followed (***stage III***). During this stage, only minor changes in Bragg peak intensities/areas were observed (Fig. 1b and Fig. 2). The final stage of the reaction -***stage IV***- started after about 8.3 h. During this stage a secondary growth in the monohydrocalcite Bragg peak areas was observed. This growth phase lasted about 2–3 h and the peak areas reaching a stable maximum after ~11 h. This same evolution was observed for all other monohydrocalcite Bragg peaks. An PXRD examination of off-line experimental solids sampled during stage IV revealed the presence of a second, but minor phase of hydromagnesite (ICDD PDF 01-070-1177; Fig. S1). Quantitative X-ray refinement with TOPAS (Coelho, 2006) determined that its abundance was ~4.5%. The on-line time resolved WAXS patterns (Fig. 3) also revealed small hydromagnesite (1 1 0) and (0 1 1) Bragg peaks that began to grow at the onset of stage IV, in parallel with the second stage of monohydrocalcite crystallization.

Analysis of the SAXS data (Fig. 4) indicates that the Mg-ACC that formed in stage I consisted of particles with a diameter of between 40 and 60 nm in size, a size that remained constant throughout this first stage. This is consistent with particle sizes derived from the TEM imaging of the Mg-ACC particles, which indicted an average diameter of ~40 nm ($n = 100$; Fig. 5a; Table 1). However, the Mg-ACC particle diameters varied between 15 and 210 nm revealing a high degree of polydispersity. The corresponding SAED patterns revealed only diffuse rings for the Mg-ACC, confirming its poorly-ordered nature (Fig. 5d). During stage

II, a distinct scattering peak appeared in the SAXS patterns (arrows in Fig. 4a) indicating that the crystals formed in the experiment were relatively monodispersed. The position of the scattering peak in the time resolved SAXS patterns moved towards lower q with time indicting particle growth (Fig. 4a). From the position of this peak and using equation (1) the particle size of the monohydrocalcite crystals was determined (Fig. 4b). At the beginning of stage II, when the first Bragg peaks for monohydrocalcite appeared in the WAXS data (Fig. 1b and Fig. 2), the corresponding SAXS data revealed an average diameter of ~9 nm for the newly forming monohydrocalcite crystals. During the rest of stages II and III these monohydrocalcite nanocrystals grew only slightly and very slowly reaching a maximum diameter of ~15 nm after 8 h. This same trend in average particles sizes was confirmed (open symbols in Fig. 4b) through selected full pattern evaluation with GNOM (Svergun, 1992). TEM microphotographs of the monohydrocalcite that formed in stage II and persisted throughout stage III (Fig. 5b) revealed that the monohydrocalcite consisted of nanocrystals, which exhibited sub-spherical to slightly elongated morphologies. Their average dimensions were 28 ± 7 (L) $\times$ 20 ± 5 (W) nm, with the minimum size being around 14×10 nm ($n = 100$). The corresponding SAED pattern showed diffraction rings with only poorly developed spots (Fig. 5e), evidencing the presence of very small but crystalline nanocrystals. At the onset of stage IV, and simultaneously with the secondary growth in Bragg peak areas for monohydrocalcite, the SAXS data also revealed a steady increase in the monohydrocalcite nanocrystal diameters, which reached a maximum of ~45 nm at the end of the reaction. Photomicrographs of a sample obtained after 10 h (stage IV; Fig. 5c) showed euhedral or subhedral single monohydrocalcite crystals with sizes of 77 ± 20 (L) $\times$ 47 ± 10 (W) nm. Again large variations in dimensions were observed, with the largest and smallest crystals being 155×80 and 40×30 nm ($n = 100$). SAED pattern from these crystals exhibited clearly defined spots within the diffraction rings (Fig. 5f). HR-TEM images of the sample taken from the end of stage IV (Fig. 5c, white arrow) revealed the presence of hydromagnesite as a minor phase consisting

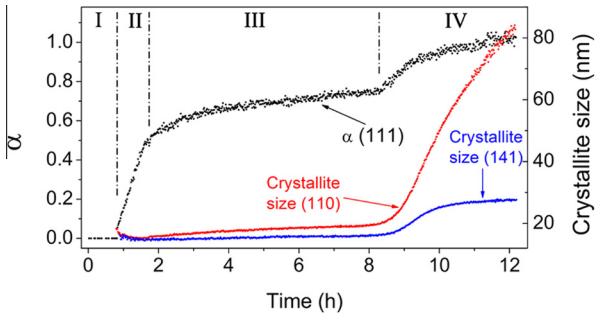

Fig. 2. Evolution of the degree of reaction (α) of the monohydrocalcite (1 1 1) Bragg peak (black symbols). The same growth profiles are true for all other Bragg peaks. Shown also with the right-hand y-axis are Scherrer crystallite sizes for the (1 1 0) and (1 4 1) peaks of monohydrocalcite as a function of time as derived from the WAXS data. I to IV correspond to the crystallization stages described in the text.

of ~100 × 5 nm platy crystals, confirming the WAXS and PXRD observations (Fig. 3 and Fig. S1).

Evaluating the corresponding WAXS patterns for the Scherrer crystallite size (Fig. 2) showed a reasonable agreement with the particle size determined from the SAXS and TEM data, and also confirmed that the forming monohydrocalcite crystals were anisotropic. For example, based on the Bragg peak (1 1 0) the data reveals that the monohydrocalcite crystals formed during stage II had a crystallite size of ~15 nm, increasing to ~20 nm during stage III, which is in agreement with the particle sizes derived from the SAXS and TEM data. Once stage IV of the crystallization was initiated, the monohydrocalcite nanocrystallite size steadily increased to >80 nm, which is almost double the average particle size from SAXS, but closer to that derived from the TEM data. However, although this general trend was the same in all other Bragg peaks, the crystallite sizes in all stages were dramatically different between the different Bragg peaks. For example, the final crystallite size from the (1 4 1) peak at the end of stage 3 was 16 nm, half that of the (1 1 0) peak, and at the end of the reaction it only reached a value of 28 nm (Fig. 2), almost three times smal-

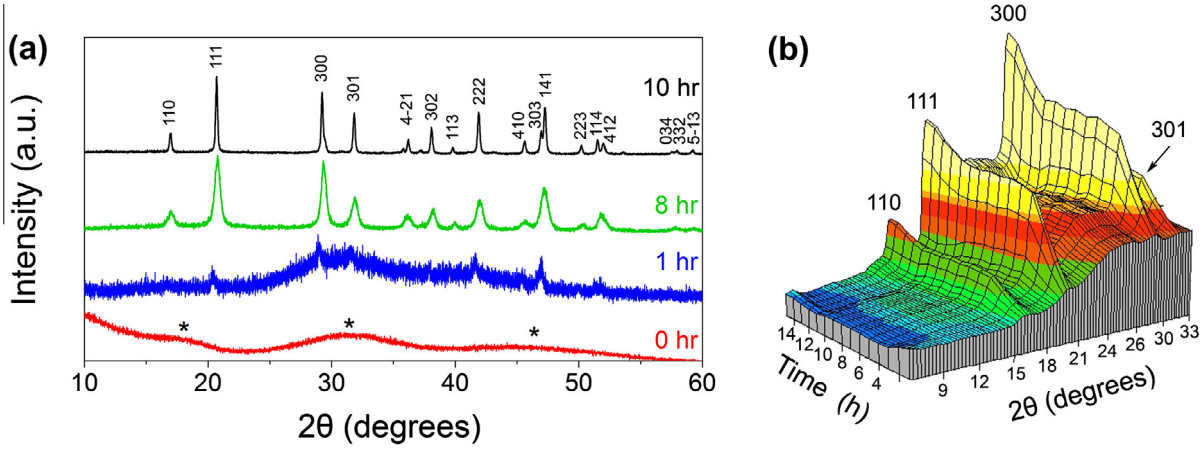

Fig. 1. (a) PXRD patterns from off-line crystallization experiments with samples removed from each run after 0, 1, 8 and 10 h. (b) 3D WAXS plot showing the time resolved formation of monohydrocalcite from the on-line experiment with only some major peaks shown.

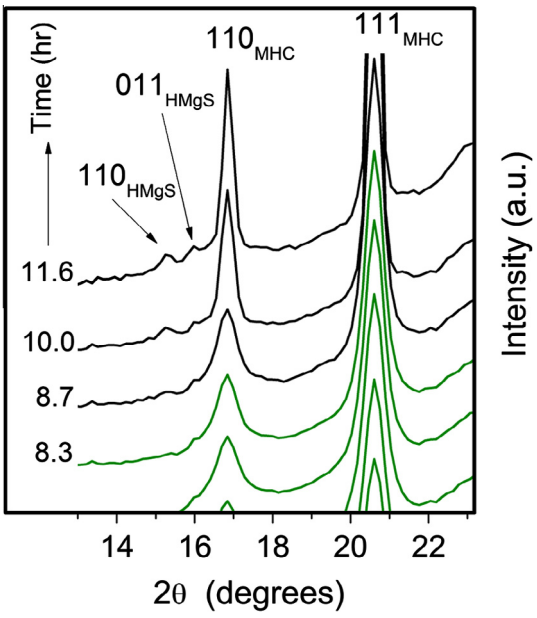

Fig. 3. Selected WAXS patterns from the on-line experiment showing the growth of the monohydrocalcite (MHC) (1 1 0) and (1 1 1) Bragg peaks and the formation of the small hydromagnesite (HMgS) (1 1 0) and (0 1 1) Bragg peaks during stages III (green patterns) and IV (black patterns) of the reaction. (For interpretation of the references to colour in this figure legend, the reader is referred to the web version of this article.)

ler than the final crystallite size from the (1 1 0) peak, indicating a clear anisotropic growth of the monohydrocalcite nanocrystals. This is consistent with the elongated particle morphology observed by TEM.

Analysis of the WAXS data also revealed changes in unit cell dimensions during the formation of monohydrocalcite (Fig. 6). Once formed, the unit cell volume (721.6 $Å^3$) remained virtually constant during stages II-III with a slight decrease during stage IV ($\Delta V \approx -0.2$ $Å^3$; Fig. 6a). However, more substantive changes were observed in the *a* and *c* axis dimensions (Fig. 6b and c, respectively). Their evolution mirrored each other, with the *a*-axis decreasing and the *c*-axis increasing in length ($\Delta c = -\Delta a \approx 0.02$ Å). These changes were small during stages II and III, but became more significant during the secondary monohydrocalcite crystallization (stage IV).

The changes in solution and solid phase chemistry during the formation and crystallization of monohydrocalcite showed a clear link between the evolution of pH, $[Ca^{2+}_{aq}]$ $[Mg^{2+}_{aq}]$ and molar fraction of Mg in the solids (Fig. 7) over the four stage of the reaction. The reaction started with a pH of 11.60 (the pH of the initial Na_2CO_3 solution), which upon mixing with the Ca/Mg solution rapidly dropped to 9.17. During stage I the pH increased slightly reaching a value of 9.24, while the formation of monohydrocalcite in stage II did not change the pH. In stage III only a small decrease in pH to a value of 9.16 was evident. However, at the end of stage III and during stage IV the pH dropped dramatically to 8.65. The $[Ca^{2+}_{aq}]$ was 1.25 mM during stage I and decreased to ≈ 0.6 mM by stage III. It then decreased further reaching a concentration <0.1 mM at the end of stage IV (Fig. 7). $[Mg^{2+}_{aq}]$ was 28 mM during stages I and II, but increased by ~20% to 35 mM during stage III. During stage IV it decreased by 40% to 13 mM. These changes in $[Mg^{2+}_{aq}]$ were mirrored throughout the whole reaction by the change in χ_{MgCO3} in the solids (Fig. 7). Furthermore, the timing of these changes in aqueous composition were all coupled with the increase in monohydrocalcite particle size (Figs. 4 and 5) and formation of hydromagnesite (Fig. 3).

From the χ_{MgCO3} values and the TGA results, the formula of the stage II monohydrocalcite was derived to be $Ca_{0.74}Mg_{0.26}CO_3{\cdot}0.99H_2O$. However, although the total χ_{MgCO3} increased during stage IV (Fig. 7), this does not represent the Mg in monohydrocalcite but primarily the contri-

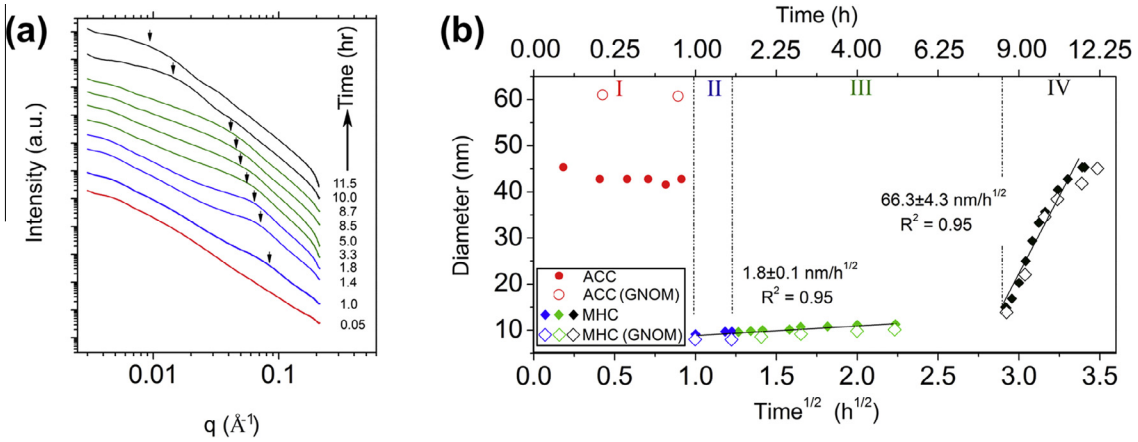

Fig. 4. (a) Double logarithmic plot showing selected SAXS patterns from the on-line *in* situ experiment with arrows indicating a changing position of the scattering peak, reflecting the growth of monohydrocalcite particles with time; colours of the patterns matches the colour code of the four stages of reaction shown in (b) Time evolution of the particle diameters for the initial amorphous phase (Mg-ACC stage I, red symbols) and for monohydrocalcite (MHC stages II to IV, blue, green and black symbols respectively) as derived from the SAXS data. Empty symbols correspond to GNOM code (Svergun, 1992). The differences in growth rates of the monohydrocalcite particles are evidenced by the fit in stages II-III and IV. (For interpretation of the references to colour in this figure legend, the reader is referred to the web version of this article.)

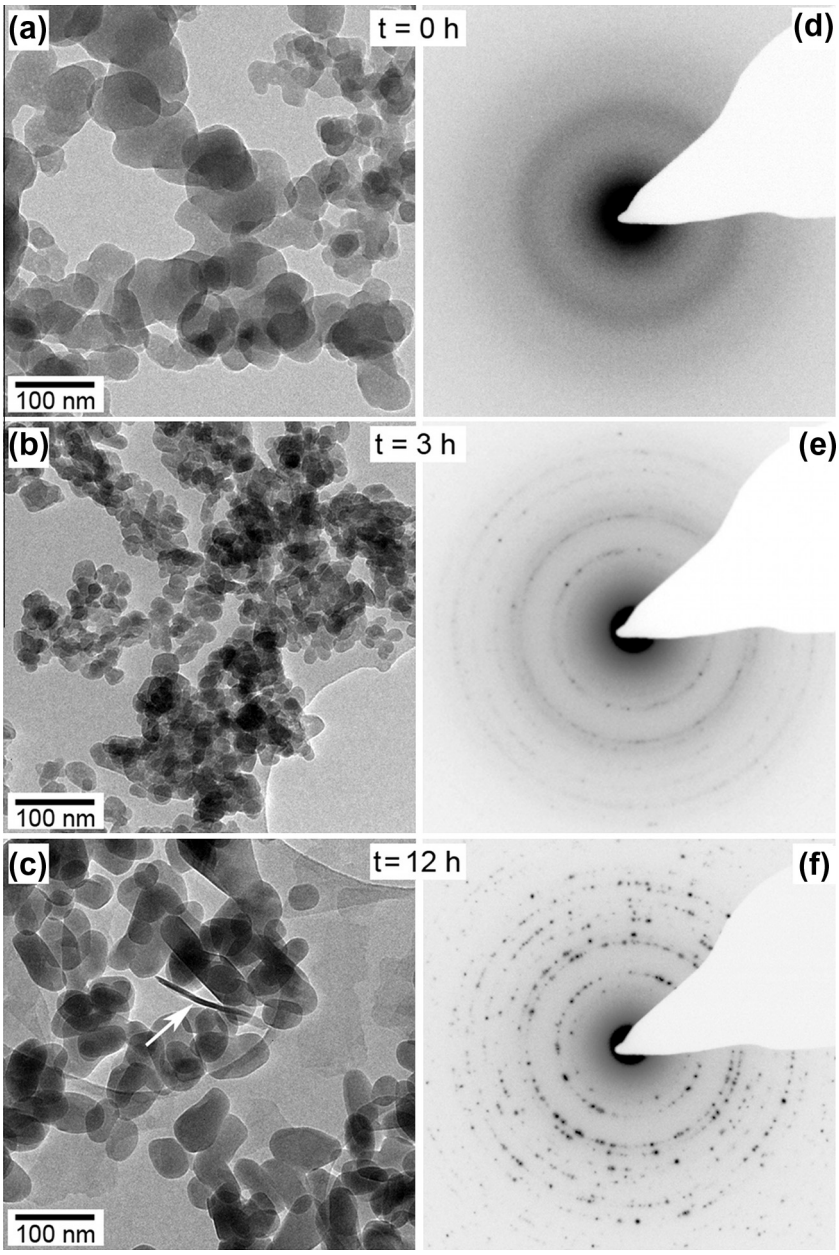

Fig. 5. HR-TEM microphotographs and corresponding SAED patterns of solids during the crystallization reaction. (a, d) Mg-ACC precursor; stage I); (b, e) Monohydrocalcite nanocrystals from stage III; (c, f) Bigger monohydrocalcite particles and a platy hydromagnesite crystal (white arrow) from the end of stage IV.

bution from the minor (~4.5%) hydromagnesite ($Mg_5(CO_3)_4(OH)_2{\cdot}4H_2O$). Using the quantitative XRD results and the composition of the final solid obtained from chemical analysis ($\chi_{MgCO3} = 0.26$, Table 1) we calculated that the molar fraction of Mg in monohydrocalcite at the end of stage IV was only ~0.065 mol, which is a 75% decrease compared to the Mg content of the stage II monohydrocalcite (0.26 mol). The remaining Mg was transferred into the newly formed hydromagnesite.

One last line of evidence that supports the observations above is the evolution of the saturation states during the reaction. PHREEQC modeling of the solution during the reaction showed that immediately after the precipitation of Mg-ACC upon mixing, the aqueous solution was supersaturated with respect to both monohydrocalcite and hydromagnesite (Fig. 8) and that the SI for both phases varied little during stages I to III ($SI_{MHC} \approx 0.5$; $SI_{HMgS} \approx 6$). The biggest change in both SI occurred at the onset of stage IV, where SI_{MHC} became undersaturated (≈ -0.85) while SI_{HMgS} dropped to ≈ 0.2. This change in SI was concomitant with the removal of Mg from solution and the associated drop in pH, due to the formation of hydromagnesite. There are however, two factors that need to be taken into account when SI_{MHC} is calculated. Firstly, two solubility products for monohydrocalcite are available in the literature: $10^{-7.60}$ (Hull and Turnbull, 1973), and

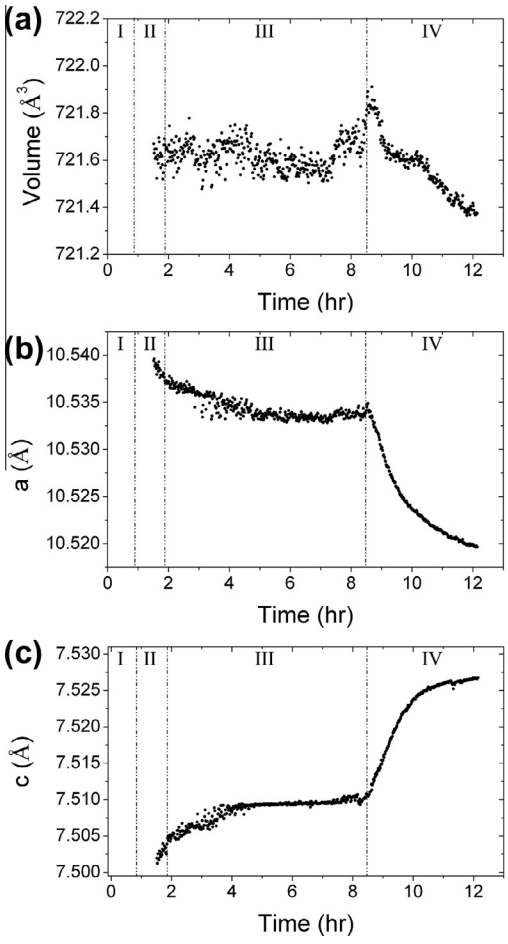

Fig. 6. Evolution of the unit cell volume (a) and of the *a* and *c* parameters (panels b and c) for monohydrocalcite over time as derived from the on-line WAXS data for stages II to IV.

$10^{-7.05}$ (Kralj and Brecevic, 1995) and this results in a ~0.55 difference in the calculated SI_{MHC} (Fig. 8). Secondly, the total ionic strength in our experiments was high (⩽1 M) and thus even an error of 1% in the ionic strength of the starting solution could also result in variations up to ~0.5 units in the calculated SI_{MHC}.

3.1. Stability of the precursor Mg-ACC and the mechanism of monohydrocalcite nucleation and growth

The formation of monohydrocalcite proceeded, in all our experiments, through a poorly-ordered Mg-ACC precursor, which precipitated from solutions with an initial $[Ca^{2+}_{aq}]$:$[Mg^{2+}_{aq}]$ of 7:3. The resulting phase was considerably more stable (crystallization started at ~50 min) compared to pure ACC (no Mg; crystallization started <2 min; Ogino et al., 1987; Rodriguez-Blanco et al., 2011, 2012; Bots et al., 2012), or Mg-ACC formed in a solution with $[Ca^{2+}_{aq}]$:$[Mg^{2+}_{aq}]$ of 9 to 1 (crystallized to calcite within ~14 min; Rodriguez-Blanco et al., 2012). However, the Mg-ACC in the current study was less stable than Mg-ACC produced from solutions where 50% of the calcium was replaced with magnesium (i.e., $[Ca^{2+}_{aq}]$:$[Mg^{2+}_{aq}]$ = 1:1), which did not crystallize at ambient temperatures even after longer reaction times (>1 day; Rodriguez-Blanco et al., 2009). The increasing stability of ACC with increasing Mg contents is not unexpected, and confirms both abiotic (Ajikumar et al., 2005; Rodriguez-Blanco et al., 2011, 2009) and biotic (Loste et al., 2003; Raz et al., 2003; Politi et al., 2010) data that demonstrate the importance of Mg in stabilizing amorphous precursors and delaying crystallization. The most likely cause of these effects is the high dehydration energy of the Mg-aquo ion compared to the Ca ion (di Tommaso and de Leeuw, 2010). Hydrated and poorly-ordered ACC is less thermodynamically stable than the dehydrated and more-ordered ACC. This dehydration and local ordering in the amorphous precursor precedes its crystallization (Radha et al., 2010; Bots et al., 2012). Hydrated Mg located within the nanoporous structure of ACC (Goodwin et al., 2010) would retard its dehydration and breakdown, slowing its transformation to crystalline phases.

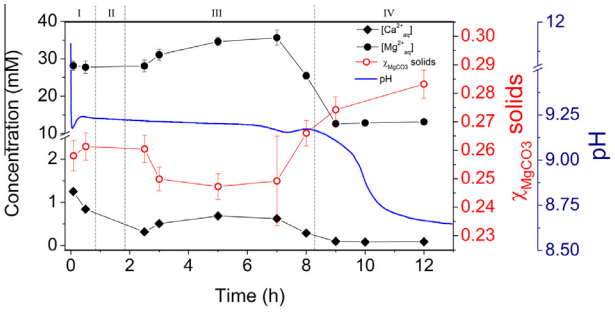

Fig. 7. Evolution of the pH, the concentrations of $[Ca^{2+}_{aq}]$, $[Mg^{2+}_{aq}]$ and of the Mg molar fraction (χ_{MgCO3}) in the solids over the course of the four stages of the crystallization reaction. Error bars correspond to the standard deviation of three measurements each.

In stage I and prior to the formation of monohydrocalcite, the pH increased by a small amount (0.07 units) (Fig. 7), which likely corresponds to the release of OH^- due to the onset of Mg-ACC dissolution. Kojima et al. (1993) showed that ACC incorporates minor amounts of OH^- ions into its structure when it forms at a basic starting pH. The Mg-ACC in our on-line experiment started forming at a pH of 11.5 (the pH of the carbonate starting

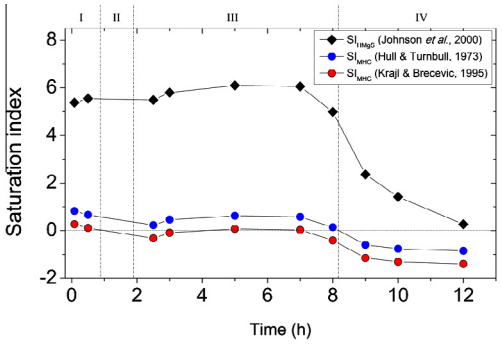

Fig. 8. Evolution of the saturation indexes for monohydrocalcite (SI_{MHC}) and hydromagnesite (SI_{HMgS}) calculated from the data shown in Fig. 7 and Table 1.

solution; Fig. 7) and thus minor OH^- in our Mg-ACC is not unexpected. Its dissolution would release OH^- ions, thus explaining the slight pH increase following:

$$Ca(OH)_{2x}(CO_3)_{1-x} \cdot yH_2O \cdot \rightarrow Ca_{1-x}(CO_3)_{1-x} + Ca^{2+}_{x,aq} + (OH)^-_{2x,aq} + yH_2O \quad (4)$$

The first monohydrocalcite crystals formed during stage II were significantly smaller than the initial Mg-ACC nanoparticles (Fig. 4b), yet once monohydrocalcite started forming, its diameter remained virtually constant throughout stage II and III. Analysis of the WAXS data shows that the amount of monohydrocalcite crystallizing increased at a constant rate throughout stage II of the reaction (Fig. 2). However, this increase was not due to particle growth (Fig. 4b) and we suggest that the formation of monohydrocalcite during stage II proceeds via the nucleation of new crystalline solids, i.e., via a nucleation-controlled reaction. The constant rate of monohydrocalcite crystallization with time (i.e., linear increase in the amount of monohydrocalcite) during most of stage II indicates a zeroth order reaction, and a constant rate of nucleation. Furthermore, the pH remained virtually constant during stage II, indicating a constant dissolution of Mg-ACC coupled with the constant nucleation of monohydrocalcite. Taking all this into account, we propose that the transformation form Mg-ACC to monohydrocalcite occurs via a simultaneous dissolution of Mg-ACC and nucleation of monohydrocalcite at a constant rate. Nucleation controlled growth has been shown for several other crystalline carbonate phases formed from amorphous Ca–Mg carbonates (e.g., vaterite and proto-dolomite; Bots et al., 2012; Rodriguez-Blanco et al., 2009). These studies suggested that the large difference in solubility between the amorphous precursor and the crystalline phases as well as the high supersaturations with respect to all crystalline phases, promotes nucleation. This nucleation process will continue until all of the amorphous precursor has been consumed, leading to a constant nucleation rate.

Stage IV of the reaction is key to understanding the effect of Mg on the formation of monohydrocalcite. The SAXS data (Fig. 4b) shows a dramatic increase in particle size. During stage IV, this increase can be fitted to a straight line when plotted as a function of $t^{1/2}$, indicating a surface-controlled Ostwald-ripening mechanism (Wagner, 1961; Tobler et al., 2009). TEM images and both WAXS and PXRD data confirm that larger and better developed monohydrocalcite crystals formed during this stage of the reaction, supporting the Ostwald-ripening mechanism. The photomicrographs of monohydrocalcites from stages III and IV (Fig. 5b and c) show an unambiguous increase in the nanocrystal sizes and a corresponding change in the SAED patterns from rings with faint spots to discrete spots, indicting an increase in particle size.

Ostwald ripening usually occurs during the later stages of crystallization reactions and involves particle growth without the formation of new material (Wagner, 1961). All nanoparticles formed in stages III are undoubtedly crystalline, but some of them are too small (<10 nm) to produce a significant amount of diffraction. Therefore scattering from these crystal is observed in the background of the PXRD/WAXS patterns during stages II and III (e.g. Fig. 1 after 1 h of reaction). This behavior is similar to that observed for ultra-small iron oxides crystallites which are too small to diffract singly (Machala et al., 2007; Ahmed et al., 2010). The intensity of the background in the XRD/WAXS patterns decreased during stages III and IV, while the Bragg peaks increased in intensity and became sharper. These changes in background and Bragg peak intensity are not due to the formation of more monohydrocalcite, but reflect the growth of the monohydrocalcite nanoparticles to a size where they diffract strongly, due to the Ostwald ripening process. The linear fits to the particle growth data with the surface-controlled growth model Fig. 4b show different rates (slopes) for the Ostwald-ripening process during stages III (slow; 1.8 ± 0.1 nm/h$^{1/2}$) and IV (fast; 66.3 ± 4.3 nm/h$^{1/2}$).

The rapid change in monohydrocalcite ripening rate is coincident with the formation of hydromagnesite; its formation lead to the fast removal of Mg from solution and triggered the rapid increase in monohydrocalcite growth rate. We suggest that structural Mg from monohydrocalcite during the ripening process was released into the solution leading to the observed increase in $[Mg^{2+}_{aq}]$ during stage III (Fig. 7). This ultimately drove the monohydrocalcite composition toward a pure $CaCO_3 \cdot H_2O$ end-member. The high concentration of Mg in solution during stage II suppressed the ripening rate, and produced a feedback effect, which decreased the rate of ripening even more (decrease in the slope of the degree of reaction plot during stage III; Fig. 2). The presence of Mg in solution is known to suppress the dissolution and growth of calcium carbonates (e.g., calcite; Mucci and Morse, 1983; Davis et al., 2000; Chen et al., 2004). Thus, is not unexpected that the high concentration of $[Mg^{2+}_{aq}]$ present during stage III significantly reduced the dissolution and reprecipitation process during the Ostwald ripening. Although the aqueous solution was supersaturated with respect to hydromagnesite throughout the reaction, this progressive increase in $[Mg^{2+}_{aq}]$ eventually triggered the nucleation of hydromagnesite at the end of stage III (Fig. 3). Its formation removed $[Mg^{2+}_{aq}]$ from solution (Fig. 7) and induced a dramatic drop in pH following:

$$4Mg^{2+} + 3HCO_3^- + 6H_2O \rightarrow \underset{\text{(hydromagnesite)}}{Mg_4(CO_3)_3(OH)_2 4H_2O} + 5H^+ \quad (5)$$

The main consequence of this Mg removal from the aqueous solution was an acceleration of the monohydrocalcite ripening reaction, which was translated into a rapid growth in particle size and the formation of highly crystalline low-Mg monohydrocalcite.

PHREEQC calculations (Table 1) also revealed that the aqueous solution was in equilibrium or slightly supersaturated with respect to nesquehonite ($Mg(HCO_3)(OH) \cdot 2(H_2O)$) during stages II and II, but became undersaturated in this mineral at stage IV. Nesquehonite was never detected using conventional XRD, synchrotron-based WAXS or HR-TEM imaging. However, Nishiyama et al. (2013) suggested that the formation of monohydrocalcite would require the paragenesis of a hydrous Mg-bearing carbonate e.g., nesquehonite, that would transform to hydromagnesite after longer reaction times. Despite the lack of experimental evidence, we can not completely discard the possibility that

small amounts of nanocrystalline nesquehonite were present during stages II and III, and that these eventually transformed to hydromagnesite during stage IV.

The inhibiting effect of Mg has been described previously for other Ca–Mg carbonates (Bischoff, 1968; Berner, 1975; Reddy and Wang, 1980; Mucci and Morse, 1983; Davis et al., 2000). For example, Zhang and Dave (2000) have suggested that the calcite growth rate is inversely proportional to the Mg concentration in solution. This effect has been attributed to the stronger hydration shell of Mg in comparison to Ca (Moomaw and Maguire, 2008; di Tommaso and de Leeuw, 2010). The higher energy, which Mg needs to dehydrate before incorporating into a carbonate structure controls the kinetics of crystal growth (Nancollas and Purdie, 1964; De Boer, 1977; Mucci and Morse, 1983). Therefore, monohydrocalcite growth would be favored at lower Mg concentrations.

3.2. Monohydrocalcite chemical and structural variability

The molar fraction of Mg in monohydrocalcite (χ_{MgCO3}) was ~0.25 during stages II and III (i.e., before the formation of hydromagnesite). This is close to the maximum values in the literature for natural or synthetic monohydrocalcites (χ_{MgCO3} = ~0.01–0.34; Brooks et al., 1950; Sapozhnikov and Tsvetkov, 1959; Marschner, 1969; Hull and Turnbull, 1973; Taylor, 1975; Skinner et al., 1977; Neumann and Epple, 2007; Nebel et al., 2008; Munemoto and Fukushi, 2008; Nishiyama et al., 2013). Many of these studies do not include information about the exact conditions at which monohydrocalcite formed (temperature, solution composition, synthesis method, etc.), therefore the factors controlling χ_{MgCO3} in monohydrocalcite are difficult to evaluate. However, we suggest that the high level of Mg in the monohydrocalcite crystallized from Mg-ACC in this study (Fig. 7) is likely due to the high supersaturation of the initial solution with respect to all carbonate phases.

To test the effect of supersaturation on the incorporation of Mg into the resulting monohydrocalcite, a set of batch experiments were performed at different initial supersaturations (Table 2). Regardless of supersaturation, immediately after mixing the initial solutions an amorphous precursor formed. Experiments with initial $SI_{MHC} > 2.43$ resulted in the crystallization of monohydrocalcite, while only Mg-calcite was obtained at lower supersaturations (Table 2 and Fig. S2). No other Ca/Mg-bearing phases were observed. PXRD analyses of the monohydrocalcite revealed that its crystallite size was inversely proportional to the starting supersaturation (Table 2), varying between 35 nm at $SI_{MHC} = 2.43$ to 16 nm at $SI_{MHC} = 3.89$. Furthermore, the χ_{MgCO3} of the monohydrocalcite increased with initial supersaturation, from 0.017 ($SI_{MHC} = 2.43$) to 0.164 ($SI_{MHC} = 3.89$, Fig. 9a). This data is consistent with previously published values for χ_{MgCO3} of synthetic monohydrocalcite produced using different initial Mg content in solution and different supersaturations (Fig. 9a; Neumann and Epple (2007), Munemoto and Fukushi (2008), however the original χ_{MgCO3} in the later reference may be higher than reported due to sample treatment). Recently, Nishiyama et al. (2013) synthesized a series of monohydrocalcites using highly variable starting $[Mg^{2+}_{aq}]/[Ca^{2+}_{aq}]/[CO_{3,aq}]$ ratios and most often an excess of carbonate, which lead to a much higher crystallization pH (9.8–11.4) compared to ours (<9.25). Their data shows that the χ_{MgCO3} in monohydrocalcite is proportional to their starting $[Mg^{2+}_{aq}]/[Ca^{2+}_{aq}]$ ratio, but these is no clear link between supersaturation and Mg contents (χ_{MgCO3}) (Fig. 9a). In addition, Nishiyama et al. (2013) used a different solution mixing approach (addition of the Na_2CO_3 solution to the $CaCl_2/MgCl_2$ solution) compared to ours (addition of the $CaCl_2/MgCl_2$ solution to the Na_2CO_3 solution). In an earlier study (Rodriguez-Blanco et al., 2012) we showed that, in the pure carbonate system, different mixing approaches lead to different initial synthesis pH, which in turn dramatically affected the crystallization pathway. Taken as a whole, both the initial $[Mg^{2+}_{aq}]/[Ca^{2+}_{aq}]/[CO_{3,aq}]$ ratios (Nishiyama et al., 2013) and initial supersaturation (this study) are key factors in controlling the Mg content of monohydrocalcite (Fig. 9a). This is also consistent with Loste et al. (2003) who showed that in other carbonate systems, precipitation at high supersaturation levels is so rapid that it results in less distinction between Ca and Mg ions. Therefore we infer that the Mg content of the solid is proportional to the initial supersaturation level and the Mg content in the initial amorphous precursor phase.

TGA analysis of the monohydrocalcite samples showed that the H_2O content (0.93–1.03 per formula unit) was similar in all solids and proportional to initial supersaturation. However, the release of structural water during heating was different depending on the molar fraction of Mg (χ_{MgCO3}) (Fig. 9b). In samples with $\chi_{MgCO3} < 0.06$ all water was released at low temperature (150–200 °C), while in the Mg-rich monohydrocalcite samples ($\chi_{MgCO3} > 0.06$) the retention of water was greater, and it was progressively released during heating to $T > 450$ °C. The final weight loss starting at 550 °C was due to carbonate decomposition. The retention of water to higher temperatures in samples with $\chi_{MgCO3} > 0.06$ is related to the greater dehydration energy (~20% higher) of Mg^{2+} in comparison to Ca^{2+} (Nancollas and Purdie, 1964; Lippmann, 1973; De Boer, 1977). Ca^{2+} and Mg^{2+} ion dehydration temperature ranges have been defined from 100–300 °C, and from 300–550 °C respectively, as the release of water associated with Mg^{2+} in the monohydrocalcite structure requires a higher temperature (300–550 °C) compared to water associated with Ca^{2+}. A detailed quantitative analysis of the TGA data (Fig. 9b, inset) shows that the amount of water released at higher temperatures (>300 °C) is directly proportional to the molar fraction of Mg in the solid.

Photomicrographs of high or low Mg-containing monohydrocalcite, reveals two distinct morphologies and sizes. Monohydrocalcite $\chi_{MgCO3} > 0.06$ consists of individual, nanometer-sized crystals that are <35 nm in size (Fig. 9c). In contrast, monohydrocalcite with $\chi_{MgCO3} < 0.06$ consists also of nanoparticulate crystallites (<35 nm), but these are aggregated to form elongated particles >5 μm in length. The morphology of these low Mg-monohydrocalcites (Fig. 9d) is identical to "type 2" spherulites described by Gránásy et al. (2005), who demonstrated that spherulitic growth occurs via growth front nucleation. This mechanism consists of the continuous nucleation of misaligned equivalent structural units on the surface of growing spherulites,

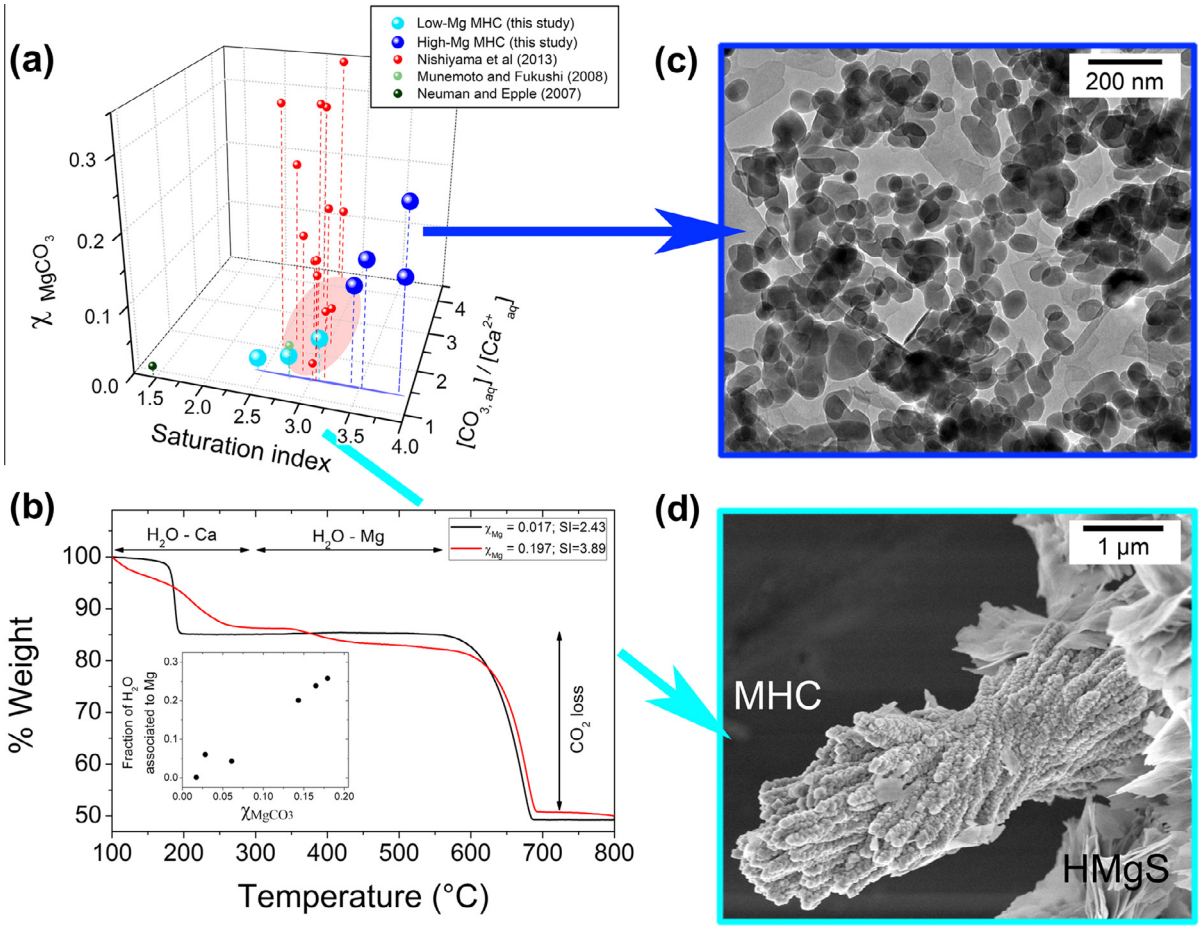

Fig. 9. (a) Three dimensional plot showing the relationship between the molar fraction of Mg (χ_{MgCO3}) in monohydrocalcite as a function of its initial saturation index (SI_{MHC}) and starting $[CO_{3,aq}]/[Ca^{2+}_{aq}]$ ratios. Blue and turquoise larger spheres are our off-line experimental data (Table 2) that were all obtained at the same starting $[CO_{3,aq}]/[Ca^{2+}_{aq}]$ ratio; the smaller, red, green and black spheres correspond to literature data. (b) Comparative TGA graphs for monohydrocalcite synthesized at high (SI = 3.89) and low (SI = 2.43) initial supersaturations (Table 2) with the inset showing the fraction of Mg-bonded structural water in monohydrocalcite *vs.* χ_{MgCO3}. Images (c) and (d) illustrate the differences in morphology, particle sizes and formation modes for our high- and low-Mg monohydrocalcite (MHC), respectively. Hydromagnesite (HMgS) crystals are also present in image (d). (For interpretation of the references to colour in this figure legend, the reader is referred to the web version of this article.)

and proceeds via unidirectional growth with low angle branching (Fig. 9d). This process is nucleation controlled with very little, if any, growth of the mineral phase. Spherulites occur in many systems (i.e., organic and inorganic), and usually require high levels of supersaturation in order drive the nucleation controlled process (Andreassen, 2005; Andreassen et al., 2010; Beck and Andreassen, 2010; Shtukenberg et al., 2012). These observations are also consistent previous studies who observed monohydrocalcite crystals with spherulitic morphologies (Duedall and Buckley, 1971; Ferguson et al., 1978; Dejehet et al., 1999; Dahl and Buchardt, 2006; Neumann and Epple, 2007; Kimura and Koga, 2011; Nishiyama et al., 2013).

Therefore, taking into account its crystal chemistry, crystallite size, thermal behavior and morphology, we propose a new categorization for monohydrocalcite:

– High-Mg monohydrocalcite ($\chi_{MgCO3} > 0.06$) consists of individual nanometer-sized crystals (<35 nm) (Fig. 9c) with a significant part (6–25%) of its structural H_2O being associated with the Mg ion, therefore displaying a progressive dehydration during heating to >500 °C (Fig. 9b). Such high-Mg monohydrocalcites are uncommon in nature, but can be synthesized in the laboratory at high initial supersaturation levels (SI > 3.25).
– Low-Mg monohydrocalcite ($\chi_{MgCO3} < 0.06$) which forms a "type 2" spherulite morphology. Less than 6% of the structural water in the low-Mg monohydrocalcite is bonded to Mg, so it fully dehydrates at low temperatures (150–200 °C). They have the same composition as natural monohydrocalcites reported in the literature, and can be synthesized in the laboratory at lower supersaturation levels (SI < 3.25).

These observations indicate that despite their different morphologies (single nanometer sized crystals and low-angle branching spherulites, respectively; Fig. 9c and d) and levels of supersaturations at which they form,

high- and low-Mg monohydrocalcite both crystallize via a nucleation-dominated growth process. The difference in particle size and morphology is likely controlled by the aqueous Mg concentration. At high concentrations, Mg poisons the formation of spherulites but still allows direct nucleation in solution, producing the non-aggregated, individual high-Mg monohydrocalcite crystals. At low supersaturations, the Mg concentration is low and monohydrocalcite forms via growth-front nucleation permitting the development of the low angle branching "type 2" spherulites.

Combining the mechanistic results described above with chemical data from our on-line experiment, and data from other studies (Fig. S3) reveals interesting relationships. Firstly, our on-line experiment shows an increase in nanocrystal sizes during the secondary crystallization of monohydrocalcite, which is coupled with a significant decrease in χ_{MgCO3} (from ~0.26 to ~0.065). This corresponds to the transition from high- to low-Mg monohydrocalcite, suggesting that the former would be metastable and rapidly transforming to the latter, possibly triggered by the removal of Mg from aqueous solution. Secondly, Davis et al. (2000) determined that the solubility of Mg-calcite ($Ca_{1-x}Mg_xCO_3$; $x = 0$–0.20) varies by approximately half an order of magnitude depending on the Mg content of the solid ($K_{sp} = 10^{-8.0}$–$10^{-8.5}$). A similar behavior should be expected for monohydrocalcite. The saturation indexes calculated for monohydrocalcite using the available solubility products from Hull and Turnbull (1973) and Kralj and Brečević (1995) are negative and show a difference of ~0.55 (Fig. 8). We suggest that may be due to difference in the Mg contents of the monohydrocalcites used in their respective studies. This hypothesis is supported by the recent findings of Nishiyama et al. (2013), who reported that the solubility of synthetic monohydrocalcite increases with higher Mg/Ca ratios in the solid. They showed that the K_{sp} of monohydrocalcite can reach maximum values of $K_{sp} = 10^{-6.77}$, which is almost one order of magnitude higher than the value of Hull and Turnbull (1973). Furthermore, Nishiyama et al. (2013) also reported an decrease in monohydrocalcite crystallite size (broadening of Bragg peaks in PXRD) with increasing solid Mg/Ca ratios, which again support our interpretation of the transition from high- to low-Mg monohydrocalcite.

Although an in-depth study of the structural changes in monohydrocalcite as a function of Mg content are outside of the scope of this study, the changes in unit cell parameters during crystallization (Fig. 6) may be better understood when the χ_{MgCO3} of the monohydrocalcite is taken into account. Regardless of Mg content, the unit cell volume remained virtually constant during stages II–III and only decreased slightly during stage IV ($\Delta V \approx -0.2$ Å^3), in parallel with the decrease in monohydrocalcite χ_{MgCO3}. This small decrease in volume is a consequence of a mirrored change in *a*-axis and *c*-axis dimensions, which may be explained by the change in the monohydrocalcite internal structure during the loss of Mg and the transition from the high to low-Mg type (stage III to IV). The structure of monohydrocalcite is less dense and more open than calcite or aragonite (Effenberger, 1981; Neumann and Epple, 2007; Swainson, 2008), therefore it may more easily adapt to a changing Mg content.

4. SUMMARY AND IMPLICATIONS

Results show that under the conditions of our study monohydrocalcite forms via a Mg-rich ACC precursor. The Mg-ACC forms rapidly then transforms to monohydrocalcite via dissolution and reprecipitation, with monohydrocalcite forming via a nucleation-controlled reaction. This crystallization path is consistent with those observed for the formation of vaterite, calcite and dolomite from (Mg-)ACC. The crystalline phase which forms from the (Mg-)ACC is controlled by the magnesium content of the precursor: pure ACC crystallizes to vaterite (Bots et al., 2012); 10% Mg-ACC crystallizes to calcite (Rodriguez-Blanco et al., 2012); ~ 30% Mg-ACC crystallizes to monohydrocalcite (this study and Nishiyama et al., 2013), and 50% Mg-ACC crystallizes to protodolomite/dolomite at higher temperatures (Rodriguez-Blanco et al., 2009). The nucleation controlled growth of these phases from ACC is thought to be due to the high solubility of (Mg-)ACC. Any solution in equilibrium with the amorphous phase will be highly supersaturated with respect to the crystalline phase, leading to nucleation controlled growth. This highlights the universal nature of the nucleation-controlled formation during crystallization from ACC.

Our results highlight the importance of Mg in the formation of monohydrocalcite. The mechanisms by which Mg controls phase stability are complex, but are related to 3 key factors. Firstly, the presence of Mg in solution is known to inhibit the formation of vaterite and calcite (Kitano and Kanamori, 1966; Bischoff, 1968; Bischoff and Fyfe, 1968; Berner, 1975; Mucci and Morse, 1983; Deleuze and Brantley, 1997; Chen et al., 2004; Bots et al., 2011). We suggest that the Mg levels in the current study (i.e. Mg/(Mg + Ca) = 0.3) were high enough to inhibit the formation of both calcite and vaterite, and favored the formation of monohydrocalcite. Secondly, the hydration shell of Mg is more strongly bound than the hydration shell of Ca (Moomaw and Maguire, 2008; di Tommaso and de Leeuw, 2010). The energy required to desolvate Mg is higher than that of Ca, a fact which explains the higher temperature required to crystallize anhydrous Ca–Mg carbonates, e.g. dolomite or magnesite (Christ and Hostettler, 1970; Lippmann, 1973; Kittrick and Peryea, 1986; Rodriguez-Blanco et al., 2009). The hydrated nature of monohydrocalcite means that full dehydration of Mg is not required before incorporation into the crystal lattice, therefore it will more likely form than the anhydrous calcium carbonate phases. The TGA analysis of the monohydrocalcite samples support this, as it shows increasing water content with Mg (Fig. 9). Thirdly, monohydrocalcite has a high capacity to accommodate Mg within its structure favoring its formation at higher Mg/Ca ratios. Thus although the initial solutions used in our work were more supersaturated with respect to all anhydrous $CaCO_3$ polymorphs, the formation of monohydrocalcite was favored.

We have shown that the crystal chemistry and growth morphology of monohydrocalcite (Stoffers and Fischbeck, 1974; Taylor, 1975; Munemoto and Fukushi, 2008) can be controlled by the initial supersaturation of the aqueous solution. We showed that with increasing supersaturation the

Mg content in the monohydrocalcite increases up to $\chi_{MgCO3} = \sim 0.26$, similar to the Mg-contents in Mg-calcites reported previously (Goldschmidt et al., 1955; Goldschmidt and Graf, 1958; Lenders et al., 2012). This has led to us defining 2 types of monohydrocalcite i.e. high-Mg and low Mg monohydrocalcite, classified according to their Mg content and morphology. All natural monohydrocalcites, which have been analyzed to date, are low Mg monohydrocalites (Mg content $\sim 0.01 > \chi_{MgCO3} < 0.075$, Hull and Turnbull, 1973; Taylor, 1975; Fukushi et al., 2011 and references therein). We suggest that the lack of high-Mg monohydrocalcite in natural environment is due to 2 factors. Firstly, for high-Mg monohydrocalcite to form, initial solutions must be extremely highly supersaturated ($SI_{MHC} \sim 3.5$–4; see Tables 1 and 2). Such extremely high supersaturation levels are difficult to achieve through natural processes. Secondly, our analysis of the monohydrocalcite crystallization pathway shows that high-Mg monohydrocalcite breaks down to low-Mg monohydrocalcite within hours of its formation, therefore high-Mg monohydrocalcite if it forms at all is likely a transient phase. Furthermore, despite monohydrocalcite not being as abundant as calcite and or aragonite in the geological record, it may still have a potential as a paleoenvironmental indicator (Solotchina et al., 2009). The isotopic composition of the hydration water in natural low-Mg monohydrocalcites may be useful as a $\delta^{18}O$ record of the paleoenvironmental conditions of the water from which it crystallized. Such an approach has been successfully applied to other hydrated carbonates like ikaite, which is even scarcer in nature and more unstable than monohydrocalcite (Rickaby et al., 2006; Lu et al., 2012).

Nevertheless, our experiments documented a simple methodology to synthesize monohydrocalcite with specific Mg/Ca ratios, specific particle sizes and shapes (i.e., reactive surface), which may have applications in a number of fields. For example, synthetic monohydrocalcite have been reported to have a high sorption capacity for PO_4^{3-} and AsO_4^{3-} (Yagi and Fukushi, 2011, 2012; Fukushi et al., 2011). Thus, by producing monohydrocalcite with specific compositions, particle sizes and shapes the effectivity of these remediation materials could be improved.

Finally, the formation of monohydrocalcite and other CaMg carbonates as a consequence of biological activity has been reported in many systems (Lowenstam, 1981; Sánchez-Román et al., 2011). Microorganisms often promote the formation of highly supersaturated microenvironments which facilitate the precipitation of carbonates (e.g., bacterial cells which absorb Ca, Mg or other metallic cations and act as nucleation sites), even when the conditions for supersaturation have not been reached in the surrounding environment (Vasconcelos and Mckenzie, 1997; Párraga et al., 1998). Systems characterized by high initial aqueous Mg/Mg + Ca values (e.g., $\geqslant 0.3$) will lead to the formation of a Mg-rich ACC precursor, which in turn will crystallize to monohydrocalcite. We suggest that this may be the primary crystallization pathway during biomineralization of monohydrocalcite.

It is interesting to note that monohydrocalcite forms at a broad range conditions in the laboratory and natural environment (i.e. a wide range of solution compositions and Mg/Ca ratios) (Fukushi et al., 2011; Wood, 2012; Nishiyama et al., 2013 and references therein). Yet, monohydrocalcite is scarce in nature, a fact that can be explained by (1) its metastability with respect to aragonite and calcite, and (2) the high supersaturation required to form it compared to other calcium carbonates. However, the chemistry of many carbonates formed during biomineralization processes indicates that they have formed from high Mg/Ca ratios seawater solutions (Reeder, 1983; Davis et al., 2000; Ries, 2004, 2010; Ries et al., 2008), and in some cases at high supersaturations (e.g., Señorale-Pose et al., 2008; Hood et al., 2011, 2012). Furthermore, the paragenesis of some mineral deposits which now contain aragonite also include a variety of Ca–Mg-bearing carbonates like dolomite, hydromagnesite or nesquehonite (Fischbeck and Müller, 1971; Broughton, 1972). Contrary to monohydrocalcite, aragonite does not necessarily require the presence of Mg to form (e.g., Ogino et al., 1987; Sand et al., 2012), but it is well known that Mg and SO_4^{2-} are the key ions responsible for the switch from calcite to aragonite seas (Sandberg, 1983; Bots et al., 2011). During geological timescales the mineralogy of most calcifying organisms was influenced by the Mg/Ca ratio of the oceans in which they evolved (Stanley, 2006; Porter, 2007). For that reason we consider that some aragonite and (Mg)-calcite deposits that are known to have formed at high Mg/Ca ratios (e.g., coralline red algal beds; rhodoliths, Schäfer et al., 2011; ooids, Davies et al., 1978; Ferguson et al., 1978; Brehm et al., 2006 or microbialites, Burne and Moore, 1987) could be secondary in origin and may have originally been a metastable monohydrocalcite intermediate which recrystallized. This secondary crystallization via monohydrocalcite could be the reason why the skeletal mineralogy and chemistry of calcareous organisms that recorded the Mg/Ca ratio of the seawater in which they grow varied so dramatically during the Phanerozoic (Ries, 2004) and this in turn may affect Mg/Ca ratio – based paleoenvironmental reconstructions. This may also explain why some early Cambrian fossils may have preferentially formed low-cost, high-Mg calcite, while later the increasing physiological cost of biomineralization lead to low Mg-calcite skeletons (Wood, 2011). Whether monohydrocalcite played a role in these early biomineralization processes is still an open question, although if monohydrocalcite was an intermediate phase during these biomineralization reactions it may have big implications for seawater chemistry reconstructions and other paleoproxies and would require further study.

ACKNOWLEDGEMENTS

This study was supported by the Marie Curie EU-FP6 Mineral Nucleation and Growth Kinetics (MIN-GRO) Research and Training Network under contract MRTNCT-2006-035488. The synchrotron work was funded via Diamond Light Source (grant numbers: SM4595 and SM1132) to Liane G. Benning.

APPENDIX A. SUPPLEMENTARY DATA

Supplementary data associated with this article can be found, in the online version, at http://dx.doi.org/10.1016/j.gca.2013.11.034.

REFERENCES

Ahmed I. A. M., Benning L. G., Kakonyi G., Sumoondur A. D., Terrill N. J. and Shaw S. (2010) Formation of green rust sulfate: a combined in situ time-resolved X-ray scattering and electrochemical study. *Langmuir* **26**, 6593–6603.

Ajikumar P. K., Wong L. G., Subramanyam G., Lakshminarayanan R. and Valiyaveettil S. (2005) Synthesis and characterization of monodispersed spheres of amorphous calcium carbonate and calcite spherules. *Cryst. Growth Des.* **5**, 1129–1134.

Andreassen J. P. (2005) Formation mechanism and morphology in precipitation of vaterite—nano-aggregation or crystal growth? *J. Cryst. Growth* **274**, 256–264.

Andreassen J. P., Flaten E. M., Beck R. and Lewis A. E. (2010) Investigations of spherulitic growth in industrial crystallization. *Chem. Eng. Res. Des.* **88**, 1163–1168.

Bateman J. E., Derbyshire G. E., Diakun G., Duxbury D. M., Fairclough J. P. A., Harvey I., Helsby W. I., Lipp J. D., Marsh A. S., Salisbury J., Sankar G., Spill E. J., Stephenson R. and Terrill N. J. (2007) The HOTWAXS detector. *Nucl. Instrum. Methods Phys. Res., Sect. A* **580**, 1526–1535.

Beck R. and Andreassen J. P. (2010) Spherulitic growth of calcium carbonate. *Cryst. Growth Des.* **10**, 2934–2947.

Berner R. A. (1975) The role of magnesium in the crystal growth of calcite and aragonite from sea water. *Geochem. Cosmochim. Acta* **39**, 489–494.

Bird M. I., Chivas A. R., Radnell C. J. and Burton H. R. (1991) Sedimentological and stable-isotope evolution of lakes in the Vestfold Hills, Antarctica. *Palaeogeogr. Palaeoclimatol.* **84**, 109–130.

Bischoff J. L. (1968) Catalysis, inhibition, and the calcite-aragonite problem – II. The vaterite-aragonite transformation. *Am. J. Sci.* **266**, 80–90.

Bischoff J. L. and Fyfe W. S. (1968) Catalysis, inhibition, and the calcite-aragonite problem: the aragonite-calcite transformation. *Am. J. Sci.* **266**, 65–79.

Bots P., Benning L. G., Rickaby R. E. M. and Shaw S. (2011) The role of SO_4 in the switch from calcite to aragonite seas. *Geology* **39**, 331–334.

Bots P., Benning L. G., Rodriguez-Blanco J. D., Roncal-Herrero T. and Shaw W. (2012) Mechanistic insights into the crystallization of amorphous calcium carbonate (ACC). *Cryst. Growth Des.* **12**, 3806–3814.

Brehm U., Krumbein W. E. and Palinska K. A. (2006) Biomicrospheres generate ooids in the laboratory. *Geomicrobiol J.* **23**, 545–550.

Brooks R., Clark L. M. and Thurston E. F. (1950) Calcium carbonate and its hydrates. *Philos. Trans. R. Soc. A* **243**, 145–167.

Broughton P. L. (1972) Monohydrocalcite in Speleothems: An Alternative Interpretation. *Contrib. Mineral. Petrol.* **36**, 171–174.

Burne R. V. and Moore L. S. (1987) Microbialites: organosedimentary deposits of benthic microbial communities. *Palaios* **2**, 241–254.

Carlström D. (1963) A crystallographic study of vertebrate otoliths. *Biol. Bull.* **125**, 441–462.

Cheary R. W. and Coelho A. (1992) A fundamental parameters approach to X-ray line-profile fitting. *J. Appl. Cristallogr.* **25**, 109–121.

Chen T., Neville A. and Yuan M. (2004) Assessing the effect of Mg^{2+} on $CaCO_3$ scale formation-bulk precipitation and surface deposition. *J. Cryst. Growth* **275**, 1341–1347.

Christ C. L. and Hostettler P. B. (1970) Studies in the system $MgO–SiO_2–CO_2–H_2O$ (II): the activity product constant of magnesite. *Am. J. Sci.* **268**, 439–453.

Coelho A. A. (2006) Topas Academic v4.1.

Dahl K. and Buchardt B. (2006) Monohydrocalcite in the arctic Ikka Fjord, SW Greenland: first reported marine occurrence. *J. Sediment. Res.* **76**, 460–471.

Davies P. J., Bubela B. and Ferguson J. (1978) The formation of ooids. *Sedimentology* **25**, 703–730.

Davis K. J., Dove P. M. and De Yoreo J. J. (2000) The role of Mg^{2+} as an impurity in calcite growth. *Science* **290**, 1134–1137.

de Boer R. B. (1977) Influence of seed crystals on the precipitation of calcite and aragonite. *Am. J. Sci.* **277**, 38–60.

de Moor P., Beelen T. P. M., Komanschek B. U., Beck L. W., Wagner P., Davis M. E. and van Santen R. A. (1999a) Imaging the assembly process of the organic-mediated synthesis of a zeolite. *Chem.-Eur. J.* **5**, 2083–2088.

de Moor P., Beelen T. P. M. and van Santen R. A. (1999b) In situ observation of nucleation and crystal growth in zeolite synthesis. A small-angle X-ray scattering investigation on Si-TPA-MFI. *J. Phys. Chem. B* **103**, 1639–1650.

Dejehet F., Idrissi S. and Debuyst R. J. (1999) Magnesium and occluded water in calcium carbonate monohydrate. *Chim. Phys.* **96**, 741–753.

Deleuze M. and Brantley S. (1997) Inhibition of calcite crystal growth by Mg^{2+} at 100 °C and 100 bars: Influence of growth regime. *Geochim. Cosmochim. Acta* **7**, 1475–1485.

Di Tommaso D. and De Leeuw N. H. (2010) Structure and dynamics of the hydrated magnesium ion and of the solvated magnesium carbonates: insights from first principles simulations. *Phys. Chem. Chem. Phys.* **12**, 894–901.

Duedall I. W. and Buckley D. E. (1971) Calcium carbonate monohydrate in seawater. *Nat. Phys. Sci.* **234**, 39–40.

Effenberger H. (1981) Kristallstruktur und infrarot-absorptionsspektrum von synthetischem monohydrocalcit, $CaCO_3·H_2O$. *Monatsh. Chem.* **112**, 899–909.

Ferguson J., Bubela B. and Davies P. J. (1978) Synthesis and possible mechanisms of formation of radial carbonate ooids. *Chem. Geol.* **22**, 285–308.

Fischbeck R. and Müller G. (1971) Monohydrocalcite, hydromagnesite, nesquehonite, dolomite, aragonite, and calcite in speleothems of the Fränkische Schweiz, Western Germany. *Contrib. Mineral. Petrol.* **33**, 87–92.

Fukushi K., Munemoto T., Sakai M. and Yagi S. (2011) Monohydrocalcite: a promising remediation material for hazardous anions. *Sci. Technol. Adv. Mater.* **12**, 064702.

Garvie L. A. J. (2003) Decay-induced biomineralization of the saguaro cactus (Carnegiea gigantea). *Am. Mineral.* **88**, 1879–1888.

Garvie L. A. J. (2006) Decay of cacti and carbon cycling. *Naturwissenschaften* **93**, 114–118.

Goldschmidt J. R. and Graf D. L. (1958) Relation between lattice constants and composition of the Ca–Mg carbonates. *Am. Mineral.* **43**, 84–101.

Goldschmidt J. R., Graf D. L. and Joensuu O. I. (1955) The occurrence of magnesian calcites in nature. *Geochim. Cosmochim. Acta* **7**, 212–230.

Goodwin A. L., Michel F. M., Phillips B. L., Keen D. A., Dove M. T. and Reeder R. J. (2010) Nanoporous structure and medium-range order in synthetic amorphous calcium carbonate. *Chem. Mater.* **22**, 3197–3205.

Gránásy L., Pusztai T., Tegze G., Warren J. A. and Douglas J. F. (2005) Growth and form of spherulites. *Phys. Rev. E* **72**, 011605.

Günther C., Becker A., Wolf G. and Epple M. (2005) In vitro synthesis and structural characterization of amorphous calcium carbonate. *Z. Anorg. Allg. Chem.* **631**, 2830–2835.

Hood A. v. S. and Wallace M. W. (2012) Synsedimentary diagenesis in a cryogenian reef complex: ubiquitous marine dolomite precipitation. *Sediment. Geol.* **255–256**, 56–71.

Hood A. v. S., Wallace M. W. and Drysdale R. N. (2011) Neoproterozoic aragonite-dolomite seas? Widespread marine

dolomite precipitation in Cryogenian reef complexes. *Geology* **9**, 871–874.

Hull H. and Turnbull A. G. (1973) A thermochemical study of monohydrocalcite. *Geochim. Cosmochim. Acta* **37**, 685–694.

Ihli J., Bots P., Kulak A., Benning L. G. and Meldrum F. C. (2012) Elucidating mechanisms of diffusion-based calcium carbonate synthesis leads to controlled mesocrystal formation. *Adv. Funct. Mater.*. http://dx.doi.org/10.1002/adfm.201201742.

Ito T. (1993) The occurrence of monohydrocalcite from calcareous sinter of cold spring of Shiowakka, Asyoro. *J. Mineral. Petrol. Econ. Geol.* **88**, 485–491.

Johnson J., Anderson G., and Parkhurst D. (2000) Database thermo.com.V8.R6.230, Rev. 1.11, Lawrence Livermore Natl. Lab., Livermore, Calif.

Kamiya K., Sakka S. and Terada K. (1977) Aragonite formation through precipitation of calcium carbonate monohydrate. *Mater. Res. Bull.* **12**, 1095–1102.

Kimura T. and Koga N. (2011) Monohydrocalcite in comparison with hydrated amorphous calcium carbonate: precipitation condition and thermal behavior. *Cryst. Growth Des.* **11**, 3877–3884.

Kitano Y. and Kanamori N. (1966) Synthesis of magnesian calcite at low temperatures and pressures. *Geochem. J.* **1**, 1–10.

Kittrick J. A. and Peryea F. J. (1986) Determination of the Gibbs free energy of formation of magnesite by solubility methods. *Soil Sci. Soc. Am. J.* **50**, 243–247.

Kojima Y., Kawanobe A., Yasue T. and Arai Y. (1993) Synthesis of amorphous calcium carbonate and its crystallization. *J. Ceram. Soc. Jpn.* **101**, 1145–1152.

Kralj D. and Brečević L. (1995) Dissolution kinetics and solubility of calcium carbonate monohydrate. *Colloids Surf., A* **96**, 287–293.

Last F. M., Last W. M. and Halden N. M. (2010) Carbonate microbialites and hardgrounds from Manito Lake, an alkaline, hypersaline lake in the northern Great Plains of Canada. *Sed. Geol.* **225**, 34–49.

Lenders J. J. M., Dey A., Bomans P. H. H., Spielmann J., Hendrix M. M. R. M., de With G., Meldrum F. C., Harder S. and Sommerdijk N. A. J. M. (2012) High-magnesian calcite mesocrystals: a coordination chemistry approach. *J. Am. Chem. Soc.* **134**, 1367–1373.

Léveillé R. J., Fyfe W. S. and Longstaffe F. J. (2000) Geomicrobiology of carbonate-silicate microbialites from Hawaiian basaltic sea caves. *Chem. Geol.* **169**, 339–355.

Lippmann F. (1973) Sedimentary carbonate minerals. In *Mineral, Rocks and Inorganic Materials* (eds. W. von Engelhardt, T. Hahn, R. Roy and P. J. Wyllie). Springer–Verlag. Berlin-Heidelberg, New York. pp. 43–96.

Loste E., Wilson R. M., Seshadric R. and Meldrum F. C. (2003) The role of magnesium in stabilising amorphous calcium carbonate and controlling calcite morphologies. *J. Cryst. Growth* **254**, 206–218.

Lowenstam H. A. (1981) Minerals formed by organisms. *Science* **211**, 1126–1131.

Lu A., Rickaby R. E. M., Kennedy H., Kennedy P., Pancost R. D., Shaw S., Lennie A., Wellner J. and Anderson J. B. (2012) An ikaite record of late Holocene climate at the Antarctic Peninsula. *Earth Planet. Sci. Lett.* **325–326**, 108–115.

Machala L., Zboril R. and Gedanken A. (2007) Amorphous iron (III) oxide – a review. *J. Phys. Chem. B* **111**, 4003–4018.

Marchal J., Tartoni N. and Nave C. (2009) Synchrotron applications of pixel and strip detectors at Diamond Light Source. *Nucl. Instrum. Methods Phys. Res., Sect. A* **604**, 123–126.

Marschner H. (1969) Hydrocalcite ($CaCO_3{\cdot}H_2O$) and nesquehonite ($MgCO_3{\cdot}3H_2O$) in carbonate scales. *Science* **165**, 1119–1121.

Moomaw A. S. and Maguire M. E. (2008) The unique nature of Mg^{2+} channels. *Physiology (Bethesda)* **23**, 275–285.

Mucci A. and Morse J. W. (1983) The incorporation of Mg^{2+} and Sr^{2+} into calcite overgrowths: influences of growth rate and solution composition. *Geochim. Cosmochim. Acta* **47**, 217–233.

Munemoto T. and Fukushi K. (2008) Transformation kinetics of monohydrocalcite to aragonite in aqueous solutions. *J. Mineral. Petrol. Sci.* **103**, 345–349.

Nancollas G. H. and Purdie N. (1964) The kinetics of crystal growth. *Q. Rev.* **18**, 1–20.

Nebel H. and Epple M. (2008) Continuous preparation of calcite, aragonite and vaterite, and of magnesium-substituted amorphous calcium carbonate (Mg-ACC). *Z. Anorg. Allg. Chem.* **634**, 1439–1443.

Nebel H., Neumann M., Mayer C. and Epple M. (2008) On the structure of amorphous calcium carbonatea detailed study by solid-state NMR spectroscopy. *Inorg. Chem.* **47**, 7874–7879.

Neumann M. and Epple M. (2007) Monohydrocalcite and its relationship to hydrated amorphous calcium carbonate in biominerals. *Eur. J. Inorg. Chem.*, 1953–1957.

Nishiyama R., Munemoto T. and Fukushi K. (2013) Formation condition of monohydrocalcite from $CaCl_2$–$MgCl_2$–Na_2CO_3 solutions. *Geochim. Cosmochim. Acta* **100**, 217–231.

Ogino T., Suzuki T. and Sawada K. (1987) The formation and transformation mechanism of calcium carbonate in water. *Geochim. Cosmochim. Acta* **51**, 2757–2767.

Onac B. P. (2000) Mineralogical studies and uranium-series dating of speleothems from Scărişoara Glacier Cave (Bihor Mountains, Romania). *Theor. Appl. Karstol.* **13**, 33–38.

Parkhurst D. L. (1995) User's guide to PHREEQC–A computer program for speciation, reaction-path, advective-transport, and inverse geochemical calculations: US Geological Survey Water-Resources Investigations, Report 95–4227. P. 143.

Párraga J., Rivadeneyra M. A., Delgado R., Iñiguez J., Soriano M. and Delgado G. (1998) Study of biomineral formation by bacteria from soil solution equilibria. *React. Funct. Polym.* **36**, 265–271.

Pitzer K. S. (1979) Theory–ion interaction approach. In *Activity Coefficients in Electrolyte Solutions, v. 1* (ed. R. M. Pytkowicz). CRC Press Inc, Boca Raton Florida, pp. 157–208.

Politi Y., Batchelor D. R., Zaslansky P., Chmelka B. F., Weaver J. C., Sagi I. S., Weiner S. and Addadi L. (2010) Role of magnesium ion in the stabilization of biogenic amorphous calcium carbonate: a structure–function investigation. *Chem. Mater.* **22**, 161–166.

Porter S. M. (2007) Seawater chemistry and early carbonate biomineralization. *Science* **316**, 1302.

Radha A. V., Forbes T. Z., Killian C. E., Gilbert P. U. P. A. and Navrotsky A. (2010) Transformation and crystallization energetics of synthetic and biogenic amorphous calcium carbonate. *PNAS* **107**, 16438–16443.

Radha A. V., Fernandez-Martinez A., Hu Y., Jun Y. S., Waychunas G. A. and Navrostsky A. (2012) Energetic and structural studies of amorphous $Ca_{1-x}Mg_xCO_3{\cdot}nH_2O$ ($0 \leqslant x \leqslant 1$). *Geochim. Cosmochim. Acta* **90**, 83–95.

Raz S., Hamilton P. C., Wilt F. H., Weiner S. and Addadi L. (2003) The transient phase of amorphous calcium carbonate in sea urchin larval spicules: the involvement of proteins and magnesium ions in its formation and stabilization. *Adv. Funct. Mater.* **13**, 480–486.

Reeder R J. (1983) Carbonates: mineralogy and chemistry. *Rev. Mineral.* (Ed. R. J. Reeder) Vol 11. 399 pp. Mineralogical Society of America.

Reddy M. M. and Wang K. K. (1980) Crystallization of calcium carbonate in the presence of metal ions. I. inhibition by magnesium ion at pH 8.8 and 25 °C. *J. Cryst. Growth* **50**, 470–480.

Rickaby R. E. M., Shaw S., Bennitt G., Kennedy H., Zabel M. and Lennie A. (2006) Potential of ikaite to record the evolution of oceanic $\delta^{18}O$. *Geology* **34**, 497–500.

Ries J. B. (2004) The effect of ambient Mg/Ca on Mg fractionation in calcareous marine invertebrates: a record of phanerozoic Mg/Ca in seawater. *Geology* **32**, 981–984.

Ries J. B. (2010) Review: geological and experimental evidence for secular variation in seawater Mg/Ca (calcite-aragonite seas) and its effects on marine biological calcification. *Biogeosciences* **7**, 2795–2849.

Ries J. B., Anderson M. A. and Hill R. T. (2008) Seawater Mg/Ca controls polymorph mineralogy of microbial $CaCO_3$: a potential proxy for calcite-aragonite seas in precambrian time. *Geobiology* **6**, 106–119.

Rivadeneyra M. A., Párraga J., Delgado R., Ramos-Cormenzana A. and Delgado G. (2004) Biomineralization of carbonates by *Halobacillus trueperi* in solid and liquid media with different salinities. *FEMS Microbiol. Ecol.* **48**, 39–46.

Rodriguez-Blanco J. D., Shaw S. and Benning L. G. (2008) How to make stable ACC: protocol and preliminary structural characterization. *Mineral. Mag.* **72**, 283–286.

Rodriguez-Blanco J. D., Shaw S. and Benning L. G. (2011) The kinetics and mechanisms of amorphous calcium carbonate (ACC) crystallization to calcite, via vaterite. *Nanoscale* **3**, 265–271.

Rodriguez-Blanco J. D., Shaw S., Bots P., Roncal-Herrero T. and Benning L. G. (2012) The role of pH and Mg on the stability and crystallization of amorphous calcium carbonate. *J. Alloy. Compd.* **536**, S477–S479.

Rodriguez-Blanco J. D., Shaw S. and Benning L. G. (2009) The realtime kinetics and mechanisms of nucleation and growth of dolomite from solution. *Geochim et Cosmochim Acta* **73**, A1111. http://dx.doi.org/10.1016/j.gca.2009.05.014.

Roncal-Herrero T., Rodríguez-Blanco J. D., Benning L. G. and Oelkers E. H. (2009) Precipitation of iron and aluminum phosphates directly from aqueous solution as a function of temperature from 50 to 200 °C. *Cryst. Growth Des.* **9**, 5197–5205.

Roncal-Herrero T., Rodríguez-Blanco J. D., Oelkers E. H. and Benning L. G. (2011) The direct precipitation of rhabdophane (REE-PO4.nH2O) from acidic aqueous solutions at 5 to 100 °C. *J. Nanopart. Res.* **13**, 4049–4062.

Sánchez-Román M., McKenzie J. A., Rebello Wagener A. L., Romanek C. S., Sánchez-Navas A. and Vasconcelos C. (2011) Experimentally determined biomediated Sr partition coefficient for dolomite: significance and implication for natural dolomite. *Geochim. Cosmochim. Acta* **75**, 887–904.

Sand K. K., Rodriguez-Blanco J. D., Makovicky E., Benning L. G. and Stipp S. L. S. (2012) Crystallization of $CaCO_3$ in water–alcohol mixtures: spherulitic growth, polymorph stabilization, and morphology change. *Cryst. Growth Des.* **12**, 842–853.

Sandberg P. A. (1983) An oscillating trend in Phanerozoic non-skeletal carbonate mineralogy. *Nature* **305**, 19–22.

Sapozhnikov D. G. and Tsvetkov A. J. (1959) Precipitation of hydrous calcium carbonate on the bottom of Lake Issyk-Kul. *Dokl. Akad. Nauk SSSR* **124**, 402–405.

Schäfer P., Fortunato H., Bader B., Liebetrau V., Bauch T. and Reuijmer J. G. J. (2011) Growth rates and carbonate production by coralline red algae in upwelling and non-upwelling settings along the Pacific coast of Panama. *Palaios* **26**, 420–432.

Scherrer P. (1918) Estimation of the size and internal structure of colloidal particles by means of röntgen. Nachr Ges Wiss Götingen. *Math-Pys. Kl.* **2**, 96–100.

Señorale-Pose M., Chalar C., Dauphin Y., Massard P., Pradel P. and Marín M. (2008) Monohydrocalcite in calcareous corpuscles of Mesocestoides corti. *Exp. Parasitol.* **118**, 54–58.

Shtukenberg A. G., Punin Y. O., Gunn E. and Kahr B. (2012) Spherulites. *Chem. Rev.* **112**, 1805–1838.

Skinner H. C. W., Osbaldiston G. W. and Wilner A. N. (1977) Monohydrocalcite in a guinea pig bladder stone, a novel occurrence. *Am. Mineral.* **62**, 273–277.

Solotchina E. P., Prokopenko A. A., Kuzmin M. I., Solotchin P. A. and Zhdanova A. N. (2009) Climate signals in sediment mineralogy of Lake Baikal and Lake Hovsgol during the LGM-Holocene transition and the 1-Ma carbonate record from the HDP-04 drill core. *Quatern. Int.* **205**, 38–52.

Stanley S. M. (2006) Influence of seawater chemistry on biomineralization throughout Phanerozoic time: paleontological and experimental evidence. *Palaeogeogr. Palaeoclimatol.* **232**, 214–236.

Stoffers P. and Fischbeck R. (1974) Monohydrocalcite in the sediments of Lake Kivu (East Africa). *Sedimentology* **21**, 163–170.

Svergun D. (1992) Determination of the regularization parameter in indirect-transform methods using perceptual criteria. *J. Appl. Crystallogr.* **25**, 495–503.

Swainson I. P. (2008) The structure of monohydrocalcite and the phase composition of the beachrock deposits of Lake Butler and Lake Fellmongery, South Australia. *Am. Mineral.* **93**, 1014–1018.

Taylor G. F. (1975) The occurrence of monohydrocalcite in two small lakes in the South-East of South Australia. *Am. Mineral.* **60**, 690–697.

Tobler D. J., Shaw S. and Benning L. G. (2009) Quantification of initial steps of nucleation and growth of silica nanoparticles: an in-situ SAXS and DLS study. *Geochim. Cosmochim. Acta* **73**, 5377–5393.

Vallina B., Rodriguez-Blanco J. D., Brown A. P., Blanco J. A. and Benning L. G. (2013) Amorphous dysprosium carbonate: characterization, stability and crystallization pathways. *J. Nanopart. Res.* **15**, 1438.

Van Driessche A. E. S., Benning L. G., Rodriguez-Blanco J. D., Ossorio M., Bots P. and García-Ruiz J. M. (2012) The role and implications of bassanite as a stable precursor phase to gypsum precipitation. *Science* **336**, 69–72.

Vasconcelos C. and McKenzie J. A. (1997) Microbial mediation of modern dolomite precipitation and diagenesis under anoxic conditions (Lagoa Vermelha, Rio de Janeiro, Brazil). *J. Sediment. Res.* **67**, 378–390.

Wagner C. (1961) Theorie der alterung von niederschlägen durch umlösen (Ostwald-Reifung). *Z. Elektrochem. Ber. Bunsenges. Phys. Chem.* **65**, 581–591.

Wang D., Wallace A. F., De Yoreo J. J. and Dove P. M. (2009) Carboxylated molecules regulate magnesium content of amorphous calcium carbonates during calcification. *Proc. Natl. Acad. Sci. USA* **106**, 21511–21516.

Wood C. J. (2012) Amorphous Calcium Carbonate (ACC) a key biomineral precursor and an environmentally significant nanoparticle: thermal transformation analysis and the effect of magnesium doping. Unpublished BSc Thesis, University of Leeds.

Wood R. A. (2011) Paleoecology of the earliest skeletal metazoan communities: implications for early biomineralization. *Earth-Sci. Rev.* **106**, 184–190.

Yagi S. and Fukushi K. (2011) Phosphate sorption on monohydrocalcite. *J. Mineral. Petrol. Sci.* **106**, 109–113.

Yagi S. and Fukushi K. (2012) Removal of phosphate from solution by adsorption and precipitation of calcium phosphate onto monohydrocalcite. *J. Colloid Interf. Sci.* **384**, 128–136.

Zhang Y. and Dave R. A. (2000) Influence of Mg^{2+} on the kinetics of calcite precipitation and calcite crystal morphology. *Geochim. Cosmochim. Acta* **163**, 129–138.

Associate editor: F. McDermott